Dear Prof. Marsh,

Point-by-point responses to the referee comments on the manuscript tc-2014-203 "Parameterization of single-scattering properties of snow" are given below. The page and line numbers refer to the marked-up version of the revised manuscript, where deletions are marked with red and additions with blue colour. For convenience, running line numbers are used.

Sincerely, on behalf of myself and my coauthors,

Petri Räisänen

Response to comments by Bastiaan van Diedenhoven

We thank Bastiaan van Diedenhoven for his constructive comments on the manuscript. Point-by-point responses to the comments are provided below. The referee comments are written in *italic* font, and our responses in normal font.

Comment: *This paper aims to provide a parameterized set of single scattering properties for surface snow. Although the resulting model is rather ad hoc, availability of such a model would be of benefit to the snow radiation modeling community, as often still models based on perfect spherical grains are used. The paper is well-structured and clear and I recommend it for publication in The Cryosphere.*

I do have a few minor suggestions and questions for the authors to consider to improve the paper:

Page 881: line 19: It is noted that, since absorption is weak at 0.8 micron and particles are in the GO regime, the modeled phase function is only weakly sensitive to size. However, it should be noted that many of the habits in the Yang et al. database have geometries (i.e. component aspect ratios) that depend on size. This means that 1) some of the obtained fits in Figure 3 probably do somewhat depend on the chosen size distribution and 2) a combination of habits that provides a good fit given a certain size could be producing a poor fit (i.e. unrealistic phase function) when applied to another size because the different geometry. However, the droxtal that is used does not depend on size, and neither does the fractal by

Macke et al. It is unclear to me from the Yang et al. papers whether the aggregates of 10 plates have geometries that depend on size. However, that appears not to be the case, as the asymmetry parameter for non-absorbing wavelengths do not appear to depend on size (for large sizes), as they would if the geometries would significantly change with size. This is then a (unintentional?) benefit of the authors final choice of habits.

Response: This is true, and in fact not completely unintentional. The processes that determine the relationship between grain shape and size in snow are different from those in ice clouds, and therefore, size-shape relationships based on crystals in ice clouds might be misleading. We feel that at this point, it is for simplicity better to ignore the size dependence of shapes. Indeed, it also helps to keep the parameterization simpler.

Change in the manuscript: In the revised manuscript, it is noted at the end of Section 3, that the geometry of some of the habits in the Yang et al. (2013) database depens on size while that for others does not (p. 10–11, lines 244–249). Furthermore, at the end of Section 4, it is made explicit that avoiding such depedencies was one of our criteria when making the final choice of the OHC (p. 15–16, lines 378–386).

Comment: *Page 886: Equations 7 and 8: I assume the Betas are a function of size parameter x here. Please add (x) for clarity.*

Response and change in the manuscript: In fact, the β:s depend not only on the size parameter x but separately on the particle size (r_{vp}) and wavelength λ (because ice refractive index depends on λ). This is marked explicitly in the revised manuscript (p. 16, Eqs. 6 and 7).

Comment: *Page 887: line 22: I think a reference to Macke et al. (1996) would be useful here.*

Response and change in the manuscript: This reference is added in the revised manuscript (p. 17, line 430).

Comment: *Page 890: Equation 12: I replotted Fig. 1 in van Diedenhoven et al (2014) and would like to confirm that this definition of absorption parameter also results in a better overlap between the single scattering albedos at several wave-*

lengths calculated for a hexagonal crystal with aspect ratio of 1 as compared with the case using the definition of van Diedenhoven et al (2014). Thank you for this insight.

Response: This is good to know! No change is required in the manuscript.

Comment: *Page 890: Equation 13: How are the parameters in this equation determined? Are these determined using a least-squares fit?*

Response: The aim of Eq. (13) is to minimize the root-mean-square error in g. In practice, the functional form of the parameterization as well as the parameter values were determined by trial and error together with visual analysis of the data. However, we believe that the parameter values are quite close to optimal, that is, a rigorous search of the parameters would probably not improve the fit significantly.

Change in the manuscript: In the revised manuscript, it is noted that Eq. (13) is aimed at minimizing the rms error of g (p. 21, lines 516–517). A more detailed discussion of the fitting approach is, in our opinion, not warranted, on one hand in the interest of brevity, and on the other hand because the "real-world" uncertainty of the parameterization is very likely influenced more by the limitations of our dataset than the numerical inaccuracy of Eq. (13) (which is anyway quite small). Basically, this remark also applies to the other comments regarding the numerical fits below.

Comment: *Page 890-891: You state that g increases slightly with increasing size parameter x_{vp} even at non-absorbing wavelengths (in the size parameter region where the geometric optics is not yet fully valid). This is probably due to the fact the diffraction asymmetry parameter becomes increasingly less than 1 for decreasing size. I suggest adding that note if you agree.*

Response: Diffraction is certainly partly responsible for this. However, it is not necessarily the only explanation, in the case of the Yang et al. (2013) database, which utilized an "improved geometric optics method" with some refinements over the ordinary geometric optics. These refinements may (and probably do) influence how the asymmetry parameter g changes with size. An inspection of the values of g at weakly absorbing wavelengths suggested that g changes somewhat more with size than expected from diffraction alone; however, it is hard to be sure because g is not provided separately for diffraction.

Change in the manuscript: In the revised manuscript, this sentence is formulated as: "$\ldots g \ldots$ increases slightly with increasing size parameter x_{vp} even at non-absorbing wavelengths, in part because the diffraction peak becomes narrower." (p. 21, lines 519–521).

Comment: *Page 891: Equations 15 and 16: I suggest adding a reference to Macke et al. (1996).*

Response and change in the manuscript: The reference is added in the revised manuscript (p. 22, line 537).

Comment: *Page 892: Equation 19: Is there any reference for this approximation? How was it determined? Diffraction is mostly determined by the projected area of a crystal, so a parameterization in terms of x_{vp} is unexpected. It may be noted that an alternative approximation was given by Eq. 14 in van Diedenhoven et al. (2014).*

Response: No reference is given in the text, which implies that the approximation was developed by ourselves. The parameterization of g_{diff} was derived by attempting to minimize the rms errors in the logarithm of phase function $\ln P_{11}$ in near-forward directions (within a few degrees), although the choice is a bit arbitrary. The minimum in rms error is not very sharp, and furthermore, we were not able to cleanly separate the diffraction peak from the rest of the phase function because only the total phase function is provided in the Yang et al. (2013) database.

The parameterization of g_{diff} is provided in terms of x_{vp} to be consistent with the rest of the SSP parameterization. However, the size parameter defined with respect to the projected area x_p, which is physically more relevant for diffraction, is directly proportional to x_{vp} for the OHC: $x_p \approx 1.535 x_{vp}$, so that Eq. (19) may be rewritten as

$$g_{\text{diff}} = 1 - 0.60/x_{vp} = 1 - 0.921/x_p. \quad (1)$$

Compared to Eq. (14) in Diedenhoven et al. (2014), our values of g_{diff} are somewhat smaller in the size range $x_p < 100$ considered by Diedenhoven et al. We found this beneficial, however, probably because it to some extent compensates for errors incurred by approximating diffraction with a Henyey-Greenstein phase function. The only way to improve the accuracy substantially would be to parameterize the shape of the diffraction peak more rigorously, but in this case,

we consider simplicity more important. As stated in the text: *This treatment of diffraction . . . is a rough approximation, and clearly not ideal for studies of very near-forward scattering, but it serves well the current purpose. On one hand, it improves the accuracy compared to the assumption of a delta spike, and on the other hand, the HG phase function has a very simple Legendre expansion . . .*

Change in the manuscript: In the revised version, the following changes/additions are made: (1) It is noted (on p. 22, lines 538–542) that the general aim in fitting the phase function parameterization was to minimize the rms errors in the logarithm of the total phase function (lnP_{11}), as the diffraction and ray tracing parts are not available separately (in this respect, the division expressed by Eq. (14) is conceptual rather than rigorous); (2) the expression of $g_{\rm diff}$ as a function of x_p is provided in Eq. (19) (on p. 22); and (3) the parameterization of Diedenhoven et al. (2014) is referred to (p. 23, lines 550–553).

Comment: *Page 892: Equation 22: Where is this form based on? How are all parameters in this equation determined?*

Response: When deriving Eq. (22), only the first two terms of Eq. (14) were included in the phase function parameterization, with diffraction treated as explained in the manuscript. In the first phase, a fortran program was utilized for an iterative search for the best value of w_1 separately for each wavelength λ = 0.199–2.7 μm and snow grain size r_{vp} = 10–2000 μm, where "best" is defined in terms of the rms error of $\ln P_{11}$ over the whole range of scattering angles (0–180°). In practice, this rms error is strongly dominated by the ray tracing part of the phase function. In the second phase, the values of w_1 were analyzed visually, and the functional form of the w_1 parameterization was determined by a "trial and error" procedure, where the goal was to minimize the rms error in w_1. We chose to exclude cases with very strong absorption (co-albedo $\beta > 0.3$) when doing this fit, since such cases are probably of little practical importance due to the low reflectance of snow. Thus, this is not a rigorous root-mean-square fit, but most probably, quite close to optimal.

Change in the manuscript: Since explaining all of this in the paper would probably be distracting to the reader, we note in the revised manuscript only the general aim of the phase function parameterization, which was to minimize the rms errors in $\ln P_{11}$ (p. 22, lines 541–542).

Comment: *Page 894: Equation 27: How are all parameters in this equation determined?*

Response: First, the phase function residuals ($P_{\rm resid}$ in Eq. 14) were determined by subtracting the diffaction and ray tracing parts (the $P_{\rm diff}$ and $P_{\rm ray}$ terms) from the "exact" phase function P_{11} for the OHC. Second, the residuals were developed into Legendre series, for each r_{vp} and λ separately. Third, the Legendre coefficients in these series were parameterized by performing a root-mean-square fit with the LAPACK subroutine DGELS, which yielded the coefficients in Eq. (27).

Change in the manuscript: In the revised manuscript, we include the following statement (on p. 24, lines 585–586): *The parameterization coefficients c_{mn} were determined by minimizing the rms errors of a_n with the LAPACK subroutine DGELS, and they are given in Table 2*.

Comment: *Page 894: line 6: Why is the Legendre expansion replaced by a polynominal? Could the terms b_n be directly determined from a_n or are they determined by a separate fit? Does the form of Eq. 28 also ensure normalization?*

Response: The ordinary polynomial form (28) was derived by writing out the Legendre polynomials in (26), which gives directly the coefficients b_n and d_{mn}. Therefore, it is completely equivalent to (26) and also ensures normalization. It is provided because in applications which do not require the use of a Legendre expansion (e.g., Monte Carlo models), an ordinary polynomial is simpler.

Change in the manuscript: To make it absolutely clear that the two forms are equivalent, the following note is added right after Eq. (29) (on p. 25, lines 594–595): *Here, the coefficients d_{mn} were obtained directly based on the coefficients c_{mn} in Eq. (27), by writing out the Legendre polynomials in Eq. (26).*

Comment: *Page 896 and further: The phase function was parameterized as simplified parameterization and a full parameterization. An even simpler parameterization would be just taking a Henyey-Greenstein phase function with the parameterized g. I think it would be useful to show the improvement that the additional terms bring compared to using a Henyey-Greenstein phase function. The HG results could be included in Figs. 10, 12, 13 and 14.*

Response: Thank you for this very useful comment! We have tested the use of

the Henyey-Greenstein phase function, and found that it leads to substantial and systematic errors in the phase function: underestimation in the diffraction peak, otherwise overestimation at forward scattering angles up to ≈35–80° (depending on the case), and underestimation at sideward and backward scattering directions.

Change in the manuscript: In the revised manuscript, results corresponding to the Henyey-Greenstein phase function are included in Figs. 10, 13 and 14 (but, in the interest of brevity, not in Fig. 12). These results are discussed on p. 27 (lines 654–662), p. 31 (lines 748–750) and p. 32 (lines 788–791).

Comment: *Figure 2a: The images appear to show many rounded crystal edges, which are signs of melting or sublimation. This can significantly affect the optical properties. Please add a discussion about the conditions of the snow pack at the time of the measurements in section 3. Can this be considered old snow?*

Response: The blowing snow case on 23 March was preceded by heavy snowfall on 22 March, ending during the night of 23rd. The last snowfall before the March 31 blowing snow case occurred on 29 March. Consequently, the case of 23 March represents essentially new snow, while on 31 March, some snow metamorphism had occurred, and the snowpack was probably denser (although snow density was not measured). The near-surface air temperature ranged from -5 to -9°C during the 23 March event and from -18 to -20°C during March 31. The wind speeds ranged from 1 to 9 m s^{-1} on 23 March (median value 4 m s^{-1}) and from 5 to 8 m s^{-1} on 23 March (median value 7 m s^{-1}). Mainly cloudy conditions prevailed on 23 March, while 31 March was cloud-free.

It is quite possible that the rounded forms in Fig. 2a are related to sublimation, but melting is not plausible because the temperature stayed well below zero during the whole campaign.

Change in the manuscript: Discussion on weather and snow conditions is added to the beginning of Section 3 (p. 7–8, lines 160–171) in the revised manuscript. The possible role of sublimation in producing particles with rounded edges is mentioned on p. 10, lines 235–236.

Comment: *Appendix A: You might want to note that the Q_{ext} for fractals equals 2 for all sizes.*

Response and change in the manuscript: This is true, due to the use of geomet-

ric optics. A short note about this is included in the revised manuscript, not in the Appendix but in connection to the discussion of Fig. 7, which shows Q_{ext}. See p. 20, lines 493–495.

Response to comments by Referee #2

We thank Referee #2 for his/her constructive comments on the manuscript. Below, the referee comments are written in *italic* font, and our responses in normal font.

Comment:

General remarks:

The authors provide a wavelength dependent single scattering parameterization based on a optimum habit combination OHC that matches observed light scattering properties at one specific wavelength. The approach is straightforward and represents a further step towards our understanding and application of light scattering at snow particles. However, the authors arrive too quickly to some conclusions where I see a need for more discussion. I therefore recommend acceptance after major revisions.

Response: More discussion is added in the revised manuscript, as described below in our responses to the specific points raised by the Referee.

Comment:

Specific points:

page 876, line 11 - 24: I understand the approach to fit observed scattering properties to model results for certain particle shape habits at a given wavelength and to use this habit combination to calculate the scattering and absorption properties at all wavelengths. However, since the reference phase function is constructed at a non-absorbing wavelength (800 nm), the OHC is not or only to a small extend dependent on particle size (as the authors also state on page 881). It mostly depends on particle geometry. The situation is even worse since the polar nephelometer with its observation range between 15 and 162 degree scattering range excludes

the forward and backward scattering region that contain the largest information on size.

Response: We are not entirely sure if we understood this comment correctly. The phase function is very weakly sensitive to size because the size parameter is very large (geometric optics regime) and absorption is very weak. However, in our view, this insensitivity can also be viewed as a benefit: it implies that potential inaccuracy in the definition of the size distribution does not influence the choice of the OHC appreciably.

At the same time, it is true that phase function observations made at $\lambda = 800$ nm contain very little information on absorption. In this sense, it is indeed a clear limitation of our dataset that the observations are made at a single very weakly absorbing wavelength. However, we would like to emphasize that this does not make it pointless to provide a snow co-albedo parameterization (Eq. 11). Namely, as evidenced by Fig. 5b and 6b–d (figure numbers referring to the original manuscript), there is a systematic difference in absorption between non-spherical particles and spheres, the co-albedo being significantly larger for non-spherical particles, for a given volume-to-projected-area equivalent radius r_{vp}. Therefore, although we are not able to constrain the co-albedo of snow precisely (as there is scatter among the non-spherical shapes), at least we can capture the systematic difference between non-spherical shapes and spheres.

Change in the manuscript: In the revised manuscript, more discussion of this issue is added to the end of Section 5, in connection to Fig. 6 (p. 19, lines 468–479).

Comment: *879, 5: "In fact, this approach does not represent any specific roughness characteristics, but..." Very good! I appreciate this comment very much as the term "roughness" is often misused in the light scattering literature.*

Response: Thanks! No change required in the manuscript.

Comment: *879, 15: "blowing snow": Of course, details can be found in Guyot et al. (2013), however, it would be good to provide some information on how representative the observed phase functions are, i.e. homogeneity of the snow conditions, duration of the observations, ...*

Response: The blowing snow case on 23 March was preceded by heavy snowfall

on 22 March, ending during the night of 23rd. The last snowfall before the March 31 blowing snow case occurred on 29 March. Consequently, the case of 23 March represents essentially new snow, while on 31 March, some snow metamorphism had occurred, and the snowpack was probably denser (although snow density was not measured). The near-surface air temperature ranged from -5 to -9°C during thea 23 March event and from -18 to -20°C during March 31. The wind speeds ranged from 1 to 9 m s^{-1} on 23 March (median value 4 m s^{-1}) and from 5 to 8 m s^{-1} on 23 March (median value 7 m s^{-1}). Mainly cloudy conditions prevailed on 23 March, while 31 March was cloud-free. The phase functions shown in Fig. 1a are averages over the entire blowing snow events, which lasted for approximately 10 hours (8–18 UTC) on 23 March and 12 hours (12–24 UTC) on 31 March.

Change in the manuscript: Discussion on weather and snow conditions is added to the beginning of Section 3 (p. 7–8, lines 160–171) in the revised manuscript.

Comment: *880, 19–26: The authors rather quickly dismiss the scattering peak at 145 degree scattering angle as an artefact and as quantitatively irrelevant. However, if this peak is caused by photodiode problems, how can we trust the rest of the observations? Why should this be limited to an angular region around 145 degree? The authors note that non of the considered particle geometries can reproduce this feature. I suggest to search the light scattering literature to identify which particle geometry could do the job.*

Response: Firstly, we have to withdraw the photodiode explanation given in the original manuscript. While it is true that reflections by photodiodes are a possible source of inaccuracy in polar nephelometer measurements, and could possibly contribute to the 145° feature, neither the paper cited in the original manuscript (Jourdan et al. 2003) or any other paper we have found provides direct evidence that this would be responsible for the 145° feature. We must apologize for not checking this properly when preparing the original manuscript. Regarding the reliability of the PN measurements, Shcherbakov et al. (2006) (their Table 1) report an accuracy of 3–5% between 15° and 141°, but degrading to 30% at 162°, for an experimental setup with low extinction. Thus the phase function derived from PN measurements is, overall, less reliable near the backscattering direction than in near-forward and side-scattering directions.

It is in principle possible that the 145° feature is caused by snow grains, but unfortunately, we have not been able to identify an ice crystal geometry that would reproduce this feature. This feature falls between the icebow peak of spherical

ice particles near 135° and a maximum that appears for many pristine hexagonal crystals at 150–155°. One might speculate that for rounded crystals (which seem to be present in Fig. 2a), the latter peak could be displaced, but it is not at all obvious (and indeed rather unlikely) that this would result in a clear maximum near 145°. Furthermore, for oriented crystals, it would most likely be possible to find geometries that produce a maximum near 145°; however the presence of a large amount of oriented crystals in blowing snow (where the conditions are typically turbulent) seems implausible. Finally, in general, the presence of a single halo peak near 145° would be surprising, when there is no evidence of other halos in the measured phase function.

One particle type that would produce a phase function maximum at 140–145° are liquid cloud droplets with a diameter of $d \sim 10$ μm. However, we consider this an unlikely explanation due to the meteorological conditions. There was no cloud (i.e., fog) at the surface level, the air was subsaturated with respect to liquid water, and the temperature was well below 0°C in both cases. In particular, the latter case (31 March) was quite cold ($-18 \ldots -20$°C), with a relative humidity of 79–87% and cloud-free skies. It is hard to imagine how a substantial amount of liquid droplets could exist in these conditions; yet the 145° feature was clearly visible in the measured phase function also in this case.

In summary, we cannot say with certainty whether the 145° feature is a real feature caused by scattering by snow or some kind of an artifact (although the latter is perhaps more likely, given that the PN data at these angles is in general less accurate than at smaller scattering angles). Further measurements, preferably using some alternative technique, would be needed to resolve this issue. Regarding the SSP parameterization, our original statement that the 145° feature has only a small influence still holds true. Note that we did not (and do not) screen out this feature when developing the parameterization.

Change in the manuscript: A shorter version of the above discussion is added to Section 3 in the revised manuscript (p. 9–10, lines 199–220).

Reference:

Shcherbakov, V., Gayet, J.-F., Baker, B. and Lawson, P., 2006: Light scattering by single natural ice crystals. *J. Atmos. Sci.*, **63**, 1513–1525.

Comment: *881, 23 - 882, 2: I respectfully disagree with the pragmatic approach to completely ignore the observed particle shapes and to adjust the optimum habit combination purely by minimizing a light scattering cost function. The observed*

snow grains should provide some constrains on the size dependent particle shape variation, see the work by Brian Baum. The authors correctly state on 884 "Thus, the potential dependence of snow crystal shapes on their size is not considered here". I consider this as an unnecessary simplification.

Response: This is, at the same time, a well-justified suggestion and one that would be very hard to address satisfactorily. Consideration of how the shape of snow grains depends on their size would require a fundamentally different approach to the development of the parameterization. This would require (1) an analysis of how the shape of grains in (blowing) snow depends on size, (2) a parameterization of this size-shape distribution, (3) the computation of the corresponding single-scattering properties (SSPs), and (4) performing the numerical fits.

We agree that in principle, this would be the ideal solution, and this approach indeed represents the state-of-the-art for the parameterization of ice cloud single-scattering properties. However, to our knowledge, it has not been attempted for snow. The primary practical difficulty is that a very large fraction of the particles in snow are irregular. For the current samples of blowing snow, manual classification of shapes in CPI images by Guyot et al. (2013) (cited in the manuscript) suggested that more than 80% of the particles were irregular. It would be unfeasible to compute the SSPs of each irregular particle "exactly", so in practice, one would have to associate them with some habit type in available SSP databases (e.g., some aggregate type in the Yang et al. (2013) database). However, there would be much ambiguity in such an approach, and it is not clear that it would, in practice, result in a better SSP parameterization. Also, carrying out such an analysis and reworking the parameterization from "scratch" would be very laborious (well beyond a typical major revision).

It may also be noted that our approach basically follows that in Kokhanovsky and Zege (2004), where the choice of Koch fractals for approximating the scattering by snow was likewise based on phase function data only. Furthermore, our approach may be considered analogous to the widely used practice of modeling the SSPs of irregular dust particles. Instead of considering the actual dust particle shapes, shape distributions of spheroids are used operationally in a variety of applications (Dubovik et al. 2006, 2011; Levy et al. 2007 (references provided in the manuscript)), as they have been found to reasonably mimic scattering by dust.

Change in the manuscript: We keep our "pragmatic" parameterization approach also in the revised manuscript. However, discussion of this issue (along the lines

noted above) is added to the beginning of Section 4 (p. 11–12, lines 256–274) and to the end of Section 8 (p. 34–35, lines 850–856) (see also our response to the last major comment).

Comment: *Discussion of Fig. 3: From the very interesting comparison of the observed phase function to those of the individual particle geometries I get the impression that the observed 145 degree peak somewhat resembles the 150 degree peak for hexagonal shaped particles.*

Response: This is true, but this peak is consistently at slightly larger scattering angles (around 150–155°) than the 145° feature in the observed phase function.

Change in the manuscript: Regarding the maximum near 145°, it is stated on p. 9, lines 204–206 in the revised manuscript that *"... it falls between the icebow peak for spherical ice particles near 135° and a maximum seen for many pristine hexagonal shapes at 150–155° (see Fig. 3)."*

Comment: *885, discussion of Fig. 5: Fig. 5a nicely shows that there is a single 3 habit combination that fits the asymmetry parameter best, and that this is not the case for the absorption parameter, because of the rather weak absorption. It looks like there is a set of 5 to 6 3 habit combinations, which provide cost < 0.1 for the absorption parameter. Are those combinations very different from each other? In general, since absorption at 800 nm does not provide much sensitivity on particle habit, as the authors also state several times, I suggest to reconsider to remove the OPC exercise for the absorption parameter.*

Response: Figure 5a demonstrates that by using three habits, we can constrain the asymmetry parameter very well, but also that there are several three-habit combinations that yield nearly as small values of the cost function. As stated in the original manuscript, the best habit combinations include "severely rough" droxtals and strongly distorted Koch fractals, while the third habit varies from one combination to another.

Regarding absorption, there are two points to make. First, the available observations indeed yield little/no information on absorption. Second, snow grains are distinctly non-spherical, and for non-spherical particles, the ξ parameter and the co-albedo β are, in general, systematically larger than those for spheres. There is some uncertainty because the values of ξ differ between different non-spherical habits. This scatter implies that our parameterization (Eq. 11) cannot be expected

to present the co-albedo of snow precisely. Nevertheless, we think that this parameterization is useful, as it is very likely that the actual values of ξ and β are larger than those for spheres.

Change in the manuscript: In the revised manuscript, a new table (Table 1) is included, which lists explicitly the three-habit combinations with cost function below 0.1. This table is introduced on p. 15, lines 364–366, whereas the corresponding text on p. 14, lines 341–344 is deleted.

Regarding absorption, Fig. 5b an the related discussion in Section 4 (on p. 15, lines 352–363) is deleted, as the above points can be made based on Fig. 6 too. Accordingly, some more discussion of this issue is added in connection to Fig. 6 (p. 18, lines 438–444 and p. 19, lines 468–479).

Comment: *887, 8: point number 4: I totally agree! But if this is so, why going through all the effort and provide a size/wavelength parameterization that may not be representative for snow particles in general? In my view, the authors too quickly jump from a case study to a general parameterization. Other researchers will happily apply this "DISORT ready-to-use" parameterization to all kind of snow conditions without questioning its applicability.*

Response: While the accuracy may not be equally good at other wavelengths or snow grain sizes, we do anticipate that it is better than that for spheres, most probably substantially better. This is an important point, as spheres are still widely used for radiative transfer calculations involving snow, due to the simplicity of using Mie theory. By providing an easy-to-use parameterization based on the OHC, we hope to improve upon this situation. To our knowlegde, no such previous parameterization exists. In this respect, the situation for snow is much less mature than that for ice clouds, for which there are numerous SSP parameterizations available. Thus, were we not to provide this parameterization, there is an obvious risk that some/many researchers will continue to use spheres for snow, happily or unhappily!

In short, most certainly our parameterization is not perfect (no parameterization is). The key question is, whether it is *useful*. In the present situation, we believe it is. If a better parameterization based on a more comprehensive dataset is provided in future, then it is of course recommendable to start using that parameterization instead.

Change in the manuscript: The limitations of the current parameterization and

the desirability of parameterizations based on more comprehensive datasets are discussed in the concluding section in the revised manuscript (changes in text on p. 33–35, between lines 816–856). For a more detailed description, see our response to the last major comment.

Comment: *896: section 7: Don't you need to account for close-packed effects in the radiative transfer calculations?*

Response: In principle, yes, but we expect that their effect is rather small. As noted in the original manuscript (p. 876, lines 26–28): *For simplicity, close-packed effects are ignored in the calculations. It has been shown by Kokhanovsky (1998) that, at least as a first approximation, they do not have a pronounced impact on the snow reflectance.* Furthermore, the same simplification has been made in most (or even nearly all) other radiative transfer studies involving snow, at least in the solar spectral region considered in this work.

Change in the manuscript: In the revised manuscript, the sentence quoted above is moved from the Introduction (p. 5, lines 90–92) to Section 7 (p. 28, lines 673–675), where this issue is more topical.

Comment: *Conclusions: I think the authors did a good job with the technical set up of the snow light scattering parameterization, but the data basis that is used for that is simply not sufficient. Thus, the work should be more carefully treated as a case study on the effect of different shape assumptions on snow reflectance. The OHC constructed here should not get generalized (as the authors try to encourage the reader on page 902).*

Response: We agree that the data basis is rather limited. Note however, that this also applies to previous studies on the topic (e.g., the suggestion to use Koch fractals by Kokhanovsky and Zege (2004) was based on a comparison with a single phase function for laboratory-generated fairly small ice crystals — here we at least have direct phase function measurements for blowing snow).

To repeat our response above, currently many researchers still use spheres for computing the single-scattering properties of snow (as this is the easiest way to go, in the absence of parameterizations based on non-spherical snow grains). In spite of the limited data basis, we think that our statement (on p. 902, lines 14–16 of the original manuscript) "*it seems reasonable to assume that the OHC selected here provides a substantially better basis for representing the SSPs of snow than*

spheres do" is justified. Therefore we think that providing this parameterization is useful.

Change in the manuscript: In response to the Referee comments, the following changes are made in the concluding section.

- The paragraph regarding the limitations of the current work (p. 902, lines 4–13 in the original manuscript) is converted to a list, to make it more explicit (p. 33–34, lines 816–834 in the revised manuscript).
- The wording of the last paragraph in the original manuscript (p. 902, lines 14–20) is moderated a bit (see p. 34, lines 837–843 in the revised manuscript).
- A new paragraph is added, which states explicitly that the current parameterization should not be considered as the "final solution" to the representation of single-scattering properties of snow. Development of snow SSP parameterizations based on more comprehensive datasets, and ideally linking the snow grain shapes more directly to those observed, is encouraged. See p. 34–35, lines 844–856.

Comment:
minor:
882, 17: fractal geometry $\rightarrow$ *tetrahedral geometry*

Response and change in the manuscript: This is corrected (p. 12, line 289 in the revised manuscript).

Comment:
885, 17: The differences in cost function, ... with lowest cost function values... ???

Response and change in the manuscript: To avoid the repetition, this is reformulated as "The differences in cost function . . . between the best habit combinations are very small . . . " (p. 15, lines 366–369).

Other changes in the manuscript

In addition to those listed above, the following minor changes have been made in the revised manuscript:

- In the introduction, two more references have been added regarding radiative transfer simulations for snow with non-spherical particles (Tanikawa et al. 2006; Jin et al. 2008), discussed on p. 4, lines 58–65. In connection to this, the text between lines 45–75 on p. 3–4 has been slightly reorganized.

- Instead of Guyot et al. (2013), a newer reference for the CLIMSLIP measurements (Guyot et al. 2015) is cited in the revised manuscript.

- In Figure 14, the wavelength $\lambda = 2.0\ \mu$m considered in the original manuscript has been replaced by $\lambda = 2.2\ \mu$m. The reasons for this change are twofold. First, the latter wavelength is potentially more relevant for observational studies, due to its higher (but still relatively low) snow albedo ($\approx$0.11, as compared with $\approx$0.011 at $\lambda = 2.0\ \mu$m) and location in an atmospheric window region. Second, in cases with extremely low snow reflectance such as $\lambda = 2.0\ \mu$m, numerical issues related to the truncation of the phase function in DISORT can cause artificial patterns in the simulated radiance distributions. This change gives rise to some changes in the text on p. 31, lines 752–768. Also, the colour scale in both Fig. 13 and 14 was modified slightly.

- Several very small changes in language (e.g., "snow grain" is now used consistently instead of "snow crystal").

References:

Guyot, G., Jourdan, O., Olofson, F., Schwarzenboeck, A., Gourbeyre, C., Febvre, G., Dupuy, R., Bernard, C., Tunved, P., Ancellet, G., Law, K., Wobrock, W., and Shcherbakov, V., 2015: Ground based in situ measurements of arctic cloud microphysical and optical properties at Mount Zeppelin (Ny-Alesund, Svalbard), in: Proceedings of the EGU conference, Vienna, Austria, 13-17 April 2015, EGU2015-14794, *http://meetingorganizer.copernicus.org/EGU2015/EGU2015-14794.pdf*.

Jin, Z., Charlock, T. P., Yang, P., Xie, Y., and Miller, W., 2008: Snow optical properties for different particle shapes with application to snow grain size retrieval and MODIS/CERES radiance comparison over Antarctica. *Remote Sens. Environ.*,

112, 3563–3581.

Tanikawa T., Aoki, T., Hori, M., Hachikubo, A., and Aniya, M., 2006: Snow bidirectional reflectance model using non-spherical snow particles and its validation with field measurements, *EARSeL eProceedings*, **5**, 137–145, *http://www.eproceedings.org/static/vol05_2/05_2_tanikawa1.html*.

Manuscript prepared for The Cryosphere Discuss.
with version 2014/09/16 7.15 Copernicus papers of the LaTeX class copernicus.cls.
Date: 2 June 2015

Parameterization of single-scattering properties of snow

P. Räisänen[1], A. Kokhanovsky[2,3], G. Guyot[4], O. Jourdan[4], and T. Nousiainen[1]

[1]Finnish Meteorological Institute, P.O. Box 503, 00101 Helsinki, Finland
[2]EUMETSAT, Eumetsat Allee 1, 64295 Darmstadt, Germany
[3]Institute of Remote Sensing, University of Bremen, 28334 Bremen, Germany
[4]Laboratoire de Météorologie Physique (LaMP) Université Blaise Pascal/CNRS/OPGC, 24 avenue des Landais, 63177 Aubiére CEDEX, France

Correspondence to: P. Räisänen (petri.raisanen@fmi.fi)

Abstract

Snow consists of non-spherical grains of various shapes and sizes. Still, in many radiative transfer applications, single-scattering properties of snow have been based on the assumption of spherical grains. More recently, second-generation Koch fractals have been employed. While they produce a relatively flat phase function typical of deformed non-spherical particles, this is still a rather ad-hoc choice. Here, angular scattering measurements for blowing snow conducted during the CLimate IMpacts of Short-Lived pollutants In the Polar region (CLIMSLIP) campaign at Ny Ålesund, Svalbard, are used to construct a reference phase function for snow. Based on this phase function, an optimized habit combination (OHC) consisting of severely rough (SR) droxtals, aggregates of SR plates and strongly distorted Koch fractals is selected. The single-scattering properties of snow are then computed for the OHC as a function of wavelength λ and snow grain volume-to-projected area equivalent radius r_{vp}. Parameterization equations are developed for $\lambda = 0.199$–$2.7\,\mu\mathrm{m}$ and $r_{\mathrm{vp}} = 10$–$2000\,\mu\mathrm{m}$, which express the single-scattering co-albedo β, the asymmetry parameter g and the phase function P_{11} as functions of the size parameter and the real and imaginary parts of the refractive index. The parameterizations are analytic and simple to use in radiative transfer models. Compared to the reference values computed for the OHC, the accuracy of the parameterization is very high for β and g. This is also true for the phase function parameterization, except for strongly absorbing cases ($\beta > 0.3$). Finally, we consider snow albedo and reflected radiances for the suggested snow optics parameterization, making comparisons to spheres and distorted Koch fractals.

1 Introduction

Snow grains are non-spherical and often irregular in shape. Still, in many studies, spherical snow grains have been assumed in radiative transfer calculations, due to the convenience of using Mie theory. In fact, it has been shown that the spectral albedo of snow can be fitted by radiative transfer calculations under the assumption of spherical snow

grains, when the effective snow grain size is considered an adjustable parameter (i.e., determined based on albedo rather than microphysical measurements) (Wiscombe and Warren, 1980; Grenfell et al., 1994; Aoki et al., 2000). Snow albedo parameterizations used in climate models and numerical weather prediction models are often semi-empirical and do not specify the snow grain shape (for some examples, see Wang and Zeng, 2010). However, in most (if not all) physically-based albedo parameterizations that explictly link the albedo to snow grain size, spherical snow grains are assumed (Flanner and Zender, 2005; Gardner and Sharp, 2010; Aoki et al., 2011).

It is, however, well known that the single-scattering properties (SSPs) of non-spherical particles, including the single-scattering albedo ω, the phase function P_{11}, and the entire phase matrix $\mathbf{P}$, can differ greatly from those of spheres.[1] A consequence of this is that the assumed shape of snow grains has a profound effect on the bidirectional reflectance distribution function BRDF of snow (Mischenko et al., 1999; Xie et al., 2006). Furthermore, Aoki et al. (2000) showed that the modelled BRDF of snow agreed better with observations if, instead of the actual phase function for spheres, the Henyey–Greenstein (HG) phase function (Henyey and Greenstein, 1941) was assumed. The HG phase function is very smooth, while that of spheres features ice-bow and glory peaks not seen for real snow, along with very low sideward scattering. ~~Therefore, Kokhanovsky and Zege (2004) recommend~~Based on a comparison of a few shape models with phase function measurements for laboratory-generated ice crystals (Barkey et al., 2002) , Kokhanovsky and Zege (2004) recommended, instead of spheres, the use of Gaussian random spheres (Muinonen et al., 1996; Nousiainen and Muinonen, 1999) or Koch fractals (Macke et al., 1996), which both exhibit a relatively featureless phase function. Since Gaussian random spheres have several free parameters while Koch fractals have none (except for the degree of distortion, for randomized Koch fractals), Koch fractals were selected by Kokhanovsky and Zege (2004). Kokhanovsky et al. (2005, 2011) further demonstrated that the reflectance patterns computed for Koch fractals agreed reasonably

[1]While symbols and abbreviations are introduced at their first appearance, they are also listed in Table A1.

well with actual measurements for snow. Subsequently, they have been used in several studies related to remote sensing of snow grain size and snow albedo (Lyapustin et al., 2009; Negi and Kokhanovsky, 2011; Kokhanovsky et al., 2011). ~~A different non-spherical shape model was consideredby Zege et al. (2011) , who~~

Other snow grain shape models have also been considered. Tanikawa et al. (2006) suggested the use of non-spherical ice particles with rough surfaces, specifically, cylindrical particles for new snow and prolate ellipsoids for old granular snow. These choices improved the agreement with observed angular reflectance patterns, as compared to the use of spheres. Jin et al. (2008) compared anisotropic reflectance factors computed using spheres, hexagonal plates, hexagonal columns and aggregates of columns with ground-based measurements in Antarctica, finding the best agreement for the aggregate model and the largest discrepancies for spheres. Furthermore, Zege et al. (2011) tested, in their retrieval algorithm of snow grain size and soot concentration in snow, a mixture of hexagonal columns and plates with rough surfaces.

~~While~~ Overall, while it is clear that spheres are not an ideal choice for modeling the SSPs of snow, it is less clear which non-spherical model should be used. ~~Although Kokhanovsky et al. (2011) demonstrated that the reflectance patterns computed for Koch fractals agreed reasonably well with actual measurements for snow, this shape model may still be regarded as an ad-hoc choice. It was selected by Kokhanovsky and Zege (2004) based on a comparison of phase functions for a small number of shape models with phase function measurements for laboratory-generated ice crystals (Barkey et al., 2002) .~~

Kokhanovsky and Zege (2004) noted that the final decision of the shape model should be made when in situ phase function measurements for snow become available. The present paper makes a step towards this direction. We employ angular scattering measurements for blowing snow performed with a polar nephelometer (Gayet et al., 1997) during the CLimate IMpacts of Short-Lived pollutants In the Polar region (CLIMSLIP) campaign at Ny Ålesund, Svalbard ~~(?)~~ (Guyot et al., 2015) to construct a reference phase function for snow grains at the wavelength $\lambda = 0.80\,\mu\text{m}$. This phase function is used to select a new shape model

for snow, an "optimized habit combination" (OHC) consisting of severely rough (SR) droxtals, aggregates of SR plates and strongly distorted Koch fractals. The SSPs for the OHC are then computed as a function of wavelength and snow grain size, and parameterization equations are developed for the single-scattering co-albedo $\beta = 1 - \omega$, the asymmetry parameter g, and the phase function P_{11}. Such parameterizations are of substantial practical significance, as they greatly facilitate the use of the OHC in radiative transfer applications. We are not aware of any such previous parameterizations for representing the snow SSPs.

~~For simplicity, close-packed effects are ignored in this paper. It has been shown by Kokhanovsky (1998) that, at least as a first approximation, they do not have a pronounced impact on the snow reflectance.~~

The outline of this paper is as follows. First, in Sect. 2, the models used to compute the SSPs of Koch fractals, Gaussian spheres and spheres are introduced, along with the database of Yang et al. (2013) used for several other shapes. In Sect. 3, the reference phase function for snow is constructed. In Sect. 4, several shape models are compared in terms of their ability to reproduce the reference phase function, and the OHC is selected. In Sect. 5, the SSPs for the OHC are computed as a function of wavelength and snow grain size, and in Sect. 6, parameterization equations are developed. In Sect. 7, the snow SSP parameterization is applied to radiative transfer computations, and comparisons are made to spheres and Koch fractals. Finally, a summary is given in Sect. 8.

2 Shape models and single-scattering data

Here, several shape models are considered as candidates for representing the SSPs of snow. These include (1) second-generation Koch fractals, (2) Gaussian random spheres, (3) nine different crystal habits in the Yang et al. (2013) single-scattering database and, for comparison, (4) spheres. The snow grains are assumed to consist of pure ice (i.e., no impurities such as black carbon are included). The ice refractive index of Warren and Brandt (2008) is employed.

The SSPs (extinction cross section, single-scattering albedo, phase function and asymmetry parameter) of Koch fractals are simulated using the geometric optics code of Macke (1993) (see also Macke et al., 1996). Both regular and distorted Koch fractals are considered. A regular second-generation Koch fractal has 144 equilateral triangular surface elements. Distortion is simulated using a statistical approach, where for each refraction-reflection event, the normal of the crystal surface is tilted randomly around its original direction (Macke et al., 1996). The zenith (azimuth) tilt angle is chosen randomly with equal distribution between $[0, \theta^{\max}]$ ($[0, 360^\circ]$), where $\theta^{\max}$ is defined using a distortion parameter $t = \theta^{\max}/90^\circ$. Values of $t = 0$ (regular), $t = 0.18$ (distorted), and $t = 0.50$ (strongly distorted) are considered. The geometric optics solution consists of ray tracing and diffraction parts, which are combined as in Macke et al. (1996). For diffraction, the Fraunhofer (far-field) approximation is employed. Either 3 million (in Sect. 4) or 1 million (in Sect. 5) rays per case (i.e., crystal size, wavelength and degree of distortion) are used for the ray tracing part. Up to $p = 12$ ray-surface interactions per initial ray are considered (see Sect. 3A in Macke, 1993).

The SSPs of Gaussian random spheres are computed with the geometric optics code of Muinonen et al. (1996). Details of the Gaussian random sphere shape model are discussed (e.g.) in Nousiainen and McFarquhar (2004). The shape of the particles is described in terms of three parameters: the relative SD of radius σ, the power-law index ν in the Legendre polynomial expansion of the correlation function of radius (the weight of the lth degree Legendre polynomial P_l being $c_l \propto l^{-\nu}$), and the degree of truncation $l_{\max}$ for this polynomial expansion. In broad terms, increasing σ increases the large-scale non-sphericity of the particle, while decreasing ν and increasing $l_{\max}$ adds small-scale structure to the particle shape. Four values were considered for σ (0.15, 0.20, 0.25 and 0.30), four for ν (1.5, 2.0, 2.5 and 3.0), and three for $l_{\max}$ (15, 25 and 35), which yields 48 parameter combinations. A total of 1 million rays with 1000 realizations of particle shape per case were employed in the ray tracing computations. Diffraction was computed by applying the Fraunhofer approximation to equivalent cross-section spheres.

Recently, Yang et al. (2013) published a comprehensive library of SSPs of non-spherical ice crystals, for wavelengths ranging from the ultraviolet to the far infrared, and for particle maximum dimensions $d_{\max}$ ranging from 2 µm to 10 000 µm. The library is based on the Amsterdam discrete dipole approximation (Yurkin et al., 2007) for small particles (size parameter smaller than about 20) and improved geometric optics (Yang and Liou, 1998; Bi et al., 2009) for large particles. Here, single-scattering properties for nine ice particle habits in the Yang et al. (2013) database are used: droxtals, solid and hollow hexagonal columns, aggregates of 8 columns, plates, aggregates of 5 and 10 plates, and solid and hollow bullet rosettes. For each habit, the SSPs are provided for three degrees of particle surface roughness: completely smooth (CS), moderately rough (MR) and severely rough (SR). The effect of roughness is simulated in a way that closely resembles the treatment of distortion for Koch fractals: the surface slope is distorted randomly for each incident ray, assuming a normal distribution of local slope variations with a SD of 0, 0.03 and 0.50 for the CS, MR and SR particles, respectively, in Eq. (1) of Yang et al. (2013). In fact, this approach does not represent any specific roughness characteristics, but rather attempts to mimic the effects on SSPs due to non-pristine crystal characteristics in general (both roughness effects and irregularities).

For comparison, results are also shown for spheres. The SSPs of spheres are computed using a Lorenz-Mie code (de Rooij and van der Stap, 1984; Mischenko et al., 1999).

3 Observation-based phase function for blowing snow

We employ as a reference an observation-based phase function for blowing snow. The reference phase function was derived from ground-based measurements conducted during the CLIMSLIP field campaign at Ny Ålesund, Svalbard ~~(?) . The~~ (Guyot et al., 2015) , on 23 and 31 March 2012. The blowing snow case on 23 March was preceded by heavy snowfall on 22 March, ending during the night of 23rd. The last snowfall before the March 31 blowing snow case occurred on 29 March. Consequently, the case of 23 March represents essentially new snow, while on 31 March, some snow metamorphism had occurred, and the snowpack

was probably denser (although snow density was not measured). The near-surface air temperature ranged from −5 to −9 °C during the 23 March case and from −18 to −20 °C during March 31. Correspondinly, the wind speeds ranged from 1 to 9 m s^{-1} on 23 March (median value 4 m s^{-1}) and from 5 to 8 m s^{-1} on 23 March (median value 7 m s^{-1}). Mainly cloudy conditions prevailed on 23 March, while 31 March was cloud-free. The phase functions discussed below are averages over the entire blowing snow events, which lasted for approximately 10 hours (8–18 UTC) on 23 March and 12 hours (12–24 UTC) on 31 March.

The angular scattering coefficient $\Psi(\theta_s)$[µm^{-1}sr^{-1}] of blowing snow was measured with the Polar Nephelometer (PN; Gayet et al., 1997; Crépel et al., 1997) on 23 and 31 March 2012, at 31 scattering angles in the $15^\circ \leq \theta_s \leq 162^\circ$ range at a nominal wavelength of $\lambda = 0.80$ µm. The corresponding phase function $P_{11}(\theta_s)$ was obtained by normalizing $\Psi(\theta_s)$ by the volume extinction coefficient σ_{ext}:

$$P_{11}(\theta_s) = 4\pi \frac{\Psi(\theta_s)}{\sigma_{\text{ext}}}. \quad (1)$$

Here σ_{ext} was estimated from the PN data following Gayet et al. (2002), with a quoted accuracy of 25 %.

The derived phase functions are shown in Fig. 1a. There are only minor differences between the 23 March and 31 March cases. In both cases P_{11} decreases sharply from 15 to 50°, then more gradually until 127°. At larger scattering angles P_{11} rather increases slightly, with a local maximum around 145° (discussed below). Hereafter, the average over the two cases is used as a reference for the modeled phase functions:

$$P_{11}^{\text{ref}} = 0.5 \cdot \left(P_{11}^{\text{23 March}} + P_{11}^{\text{31 March}}\right). \quad (2)$$

In Fig. 1b, P_{11}^{ref} is compared with three other phase functions: a non-precipitating cirrus case over Southern France in the CIRRUS'98 experiment (Durand et al., 1998) (discussed in Jourdan et al., 2003), and two phase functions for glaciated parts of nimbostratus over Svalbard in the ASTAR 2004 experiment, corresponding to Clusters 6 and 7 in

Jourdan et al. (2010). These phase functions were derived from raw PN data using a statistical inversion scheme (Jourdan et al., 2003, 2010). Perhaps as expected, the blowing snow phase function P_{11}^{ref} is generally closer to the glaciated nimbostratus phase functions than to the cirrus phase function. In particular, at sideward angles between roughly 55° and 135°, P_{11}^{ref} falls mostly between the two nimbostratus phase functions, while the cirrus phase function exhibits somewhat smaller values. The smallest P_{11} in the cirrus and nimbostratus cases occurs at $\theta_s = 120°$, as compared with $\theta_s = 127°$ for P_{11}^{ref}. All four phase functions then increase until $\theta_s \approx 140°$, after which the nimbostratus and cirrus phase functions become quite flat. In contrast, P_{11}^{ref} shows a local maximum around $\theta_s \approx 145°$.

~~It is possible that~~ The origin of the maximum at $\theta_s \approx 145°$ is ~~an artifact. It may~~not clear. While it may, in principle, be caused by ~~light contamination due to reflection on photodiodes, which is often seen in PN measurements (Jourdan et al., 2003) . However, this feature~~ scattering by snow grains, this feature is not captured by any of the particle shapes considered in this study; nor is it present in phase functions measured for laboratory-generated ice crystals in Barkey et al. (2002) and Smith et al. (2015) . Rather, it falls between the icebow peak for spherical ice particles near 135° and a maximum seen for many pristine hexagonal shapes at 150–155° (see Fig. 3). Curiously, this feature coincides with the scattering maximum of small water droplets with a $\sim 10\,\mu$m diameter at 140–145°. However, water droplets seem like an implausible explanation, since the conditions at the measurement site were subsaturated with respect to liquid water (the relative humidity being roughly 92–95% on 23 May and 79–87% on 31 May), and especially the 31 March case was quite cold. Yet the 145° feature is clearly visible in the measured phase function in both cases. Finally, we cannot discount the possibility that inaccuracy in the PN angular scattering measurements influences this feature. Shcherbakov et al. (2006) report relative accuracy of scattered intensities of 3-5% between 15° and 141°, but degrading to 30% for 162°, for an experimental setup with low extinction. Thus the phase function derived from the PN measurements is, overall, less reliable near the backscattering direction than in near-forward and side-scattering directions.

Whether the phase function feature at 145° is an artifact or a real feature caused by scattering by snow should be resolved through further measurements, preferably using some alternative technique. However, in either case, it has only a small impact on the snow SSP parameterizations derived in this paper. This detail cannot be captured by any of the shape models considered, so it is not present in the parameterized phase functions. Its influence on the asymmetry parameter is also modest. Even a complete elimination of the maximum by linear interpolation of P_{11}^{ref} between the minima at 127° and 155° would increase g by only ≈ 0.007.

The size distribution of blowing snow was measured with the Cloud Particle Imager (CPI) instrument (Lawson et al., 2001). The CPI registers particle images on a solid state, one million pixel digital charge-coupled device (CCD) camera by freezing the motion of the particle using a 40 ns pulsed, high power laser diode. Each pixel in the CCD camera array has an equivalent size in the sample area of 2.3 µm. In the present study, the minimum size for the CPI's region of interest is set up to 10 pixels. Therefore particles with sizes ranging approximately from 25 µm to 2 mm are imaged.

Figure 2a shows examples of particles imaged by the CPI on 31 March 2012. While some needle-shaped crystals can be spotted, many of the ~~crystals~~ particles are irregular, which also applies to the 23 March 2012 case. It is also noted that many of the particles show rounded edges, possibly related to sublimation during snow metamorphosis. Size distributions derived from the CPI data are shown in Fig. 2b. A lognormal distribution was fitted to the data (averaged over the 23 and 31 March cases):

$$n(d_{\mathrm{p}}) = \frac{1}{\sqrt{2\pi}\ln\sigma_{\mathrm{g}} d_{\mathrm{p}}} \exp\left[-\frac{\left(\ln d_{\mathrm{p}} - \ln d_{\mathrm{p},0}\right)^2}{2\ln^2\sigma_{\mathrm{g}}}\right]. \tag{3}$$

Here, d_{p} is the projected-area equivalent diameter of the particles, $d_{\mathrm{p},0} = 187$ µm is the median diameter, and $\sigma_{\mathrm{g}} = 1.62$ the geometric SD. This size distribution was used for all shape models, when comparing the modeled phase functions with P_{11}^{ref}. ~~However, since~~ Since absorption is weak at $\lambda = 0.80$ µm and the particles are much larger than the wavelength, the modeled P_{11} is only weakly sensitive to the size distribution employed, if the shape

of the snow grains is independent of size. This holds true for spheres, Gaussian spheres, Koch fractals, droxtals, and the three aggregate habits in the Yang et al. (2013) database. However, for solid and hollow hexagonal columns, plates, as well as solid and hollow bullet rosettes, the crystal geometry is a function of size, with some influence on P_{11} (see end of Sect. 4 for more discussion).

4 Selecting a shape model for snow optics

The purpose of this section is to select a shape model of snow for use in Sects. 5 to 7. The phase function for blowing snow from the CLIMSLIP campaign, as defined by Eq. (2), is used as a reference. It is emphasized that the approach is deliberately pragmatic: we do not attempt to model the scattering based on the shapes of the observed snow grains, but rather try to develop an equivalent microphysical model for representing the SSPs. Previously, the choice of Koch fractals for approximating the scattering by snow (Kokhanovsky and Zege, 2004) was likewise based on phase function data only. Furthermore, our approach is conceptually analogous to the widely used practice of modeling the SSPs of irregular dust particles. Instead of considering the actual dust particle shapes, shape distributions of spheroids are used operationally in a variety of applications (Dubovik et al., 2006, 2011; Levy et al., 2007) , as they have been found to reasonably mimic scattering by dust. In contrast, current state-of-the-art models for ice cloud SSPs include ice crystal habit distributions parameterized as a function of crystal size, based on in situ microphysical observations (Baum et al., 2005, 2011; Hong et al., 2009) . In principle, it would be desirable to use this approach also for snow, to provide a more direct link between the actual snow grain shapes and those assumed in the parameterization, and to account for changes in snow grain shape with size, which we currently neglect. This would require, first, the analysis and subsequent parameterization of snow grain shape distributions as a function of size, and second, the computation and parameterization of the respective SSPs. The main reason why we have not attempted this approach in the current work is that a very large fraction of the particles in blowing snow (and snow on ground) are irregular,

more than 80% according to manual classification of CPI images (Guyot et al., 2015) (see also Fig. 2a), and cannot be unambiguously associated with habits considered (e.g) in the database of Yang et al. (2013) .

To provide a quantitative measure for the agreement between the modeled and reference phase functions (P_{11}^{model} and P_{11}^{ref}, respectively) we define a cost function as the root-mean-square error of the logarithm of phase function:

$$\text{cost} = \sqrt{\frac{\int_{15^\circ}^{162^\circ} \left(\ln P_{11}^{\text{model}} - \ln P_{11}^{\text{ref}}\right)^2 \sin\theta_s \mathrm{d}\theta_s}{\int_{15^\circ}^{162^\circ} \sin\theta_s \mathrm{d}\theta_s}}. \quad (4)$$

To start with, the phase function for single crystal shapes is compared with P_{11}^{ref} in Fig. 3. To be consistent with the CLIMSLIP observations, the phase function is computed at $\lambda = 0.80\,\mu\text{m}$, and it is integrated over the size distribution defined by Eq. (3). Several points can be noted.

First, unsurprisingly, the phase function for spheres agrees poorly with the observations (Fig. 3a). In particular, sideward scattering is underestimated drastically, and there is a strong ~~"icebow "~~ icebow peak at $\theta_s = 134^\circ$, which is not seen in P_{11}^{ref}.

Second, for 2nd generation Koch fractals (Fig. 3b), the agreement with P_{11}^{ref} is considerably better than for spheres. The main features of the phase function are similar for regular and distorted Koch fractals. However the regular Koch fractal's phase function exhibits several sharp features specific to the ~~fractal~~ tetrahedral geometry, which are not observed in P_{11}^{ref}. The distorted Koch fractals' versions are more consistent with the measurements even though marked deviations from P_{11}^{ref} are still present. Scattering is underestimated between 15 and 30° and overestimated between 45 and 100°. Also, the gradient of P_{11} in the backscattering hemisphere is consistently negative, while P_{11}^{ref} rather increases slightly between 127 and 162°. Overestimated sideward scattering by Koch fractals has been previously noted in the context of cirrus clouds (Francis et al., 1999) and in a comparison with a measured phase function for laboratory-generated ice crystals (Fig. 3 in Kokhanovsky and Zege, 2004).

Third, for Gaussian spheres, the level of agreement with P_{11}^{ref} depends on the shape parameters chosen. Four cases out of the 48 considered are shown in Fig. 3c (for all of these, $l_{\text{max}} = 15$, but the general features for $l_{\text{max}} = 25$ and $l_{\text{max}} = 35$ are similar). For example, for the parameter values $\sigma = 0.15$ and $\nu = 3.0$, which are close to those estimated from shape analysis of small quasi-spherical ice crystals in cirrus clouds in Nousiainen et al. (2011), the deviations from P_{11}^{ref} are substantial. The phase function features undesirable large-scale oscillations, and in particular, scattering at $\theta_s \approx 45$–75° is underestimated substantially. Best agreement with P_{11}^{ref} is obtained in the case $\sigma = 0.30$, $\nu = 0.15$, which features both pronounced large-scale non-sphericity and small-scale structure in the particle shape. The sideward scattering is overestimated (mainly between 70 and 100°), but the cost function (0.163) is clearly smaller than that for distorted Koch fractals (0.284), and is, in fact, the smallest among all single-habit shape models considered.

Fourth, regarding the habits in the Yang et al. (2013) database (Fig. 3d–l), both visual inspection and the cost function values indicate that the agreement with P_{11}^{ref} improves with increasing particle surface roughness. While completely smooth and, in many cases, moderately rough particles exhibit halo peaks, for severely rough particles the phase function is quite smooth and featureless, as is P_{11}^{ref}. It is further seen that in general, increasing the roughness increases sideward scattering and reduces the asymmetry parameter. While none of the habits considered provides perfect agreement with P_{11}^{ref}, the cost function is smallest for the aggregate of 8 columns (0.172).

Since none of the individual shape models agrees fully satisfactorily with P_{11}^{ref}, we considered combinations of two or three shapes. ~~Conceptually, this is analogous to the modeling of SSPs of irregular dust particles with a shape distribution of spheroids, which is used operationally in a variety of applications (Dubovik et al., 2006, 2011; Levy et al., 2007) .~~ We thus use

$$P_{11}^{\text{model}} = \sum_{j=1}^{n} w_j P_{11}^{j}, \tag{5}$$

where $n = 2$ or $n = 3$ is the number of shapes in a combination and P_{11}^{j} is the phase function for shape j, integrated over the size distribution (Eq. 3) for each shape separately. Thus, the potential dependence of snow ~~crystal~~ grain shapes on their size is not considered here. For each combination of shapes considered, the optimal weight factors w_j were searched by minimizing the cost function (Eq. 4), subject to the conditions that all w_j are non-negative and their sum equals 1. Since pristine particles and even moderately rough particles feature halo peaks (or an icebow peak in the case of spheres), which are absent in P_{11}^{ref}, the following groups of habits are considered: distorted Koch fractals, Gaussian spheres, and severely rough (SR) particles in the Yang et al. (2013) database.

Figure 4 illustrates a comparison with P_{11}^{ref} for three single-habit cases (Fig. 4a and d) (the best Koch fractal case, the best Gaussian sphere case, and the best case with Yang et al. (2013) particles), the best three two-habit cases (Fig. 4b and e) and the best three three-habit cases (Fig. 4c and f), as defined in terms of the cost function. As expected, the agreement of P_{11}^{model} with P_{11}^{ref} improves with increasing number of crystals in the combination. The best three-habit cases follow P_{11}^{ref} quite faithfully, though slightly underestimating P_{11}^{ref} in near-forward directions and not capturing the ~~(possibly artificial)~~ details of P_{11}^{ref} near $\theta_s = 145°$. Furthermore, it is seen that the best three-habit combinations produce nearly identical P_{11}, agreeing even better with each other than with P_{11}^{ref}. ~~These combinations, like most other three-habit combinations with low values of the cost function, include SR droxtals and strongly distorted Koch fractals, but the third habit included in the combinations varies from case to case.~~

The relationship between the asymmetry parameter g and the cost function is considered in Fig. 5~~a~~, where all single-habit cases and combinations of two or three habits are included. While high values of cost function can occur at any g, the lowest values (< 0.10) always occur for three-habit combinations with $0.775 < g < 0.78$. This supports a best estimate of $g \approx 0.78$ for snow at $\lambda = 0.80\,\mu\text{m}$, of course subject to the assumption that the measurements for blowing snow used to construct P_{11}^{ref} are also representative of snow on ground.

While the cost function is able to constrain g quite well, the single-scattering co-albedo β is equally important. Figure 5b shows a scatter plot of cost function vs. the non-dimensional absorption parameter (Kokhanovsky and Zege, 2004; Kokhanovsky, 2013)

$$\xi = \frac{C_{\text{abs}}}{\gamma V} = \frac{Q_{\text{ext}} P \beta}{\gamma V},$$

where C_{abs} is the absorption cross section, Q_{ext} the extinction efficiency, P the projected area and V the volume, all integrated over the size distribution, and $\gamma = 4\pi m_i/\lambda$, $m_i = 1.34 \times 10^{-7}$ being the imaginary part of the refractive index and λ=0.80the wavelength. Most values of ξ for non-spherical particles lie between 1.55 and 1.75, which is considerably higher than the value for spheres (1.29) . However, there is no obvious convergence of ξ with decreasing cost function. Thus, the cost function does not constrain ξ properly, which is expected since at λ=0.80, absorption is quite weak and has a negligible effect on the phase function.

The three-habit combinations with cost function below 0.1 are listed in Table 1. All of them include SR droxtals and either strongly distorted ($t = 0.50$) or distorted ($t = 0.18$) Koch fractals, but the third habit included in the combinations varies from case to case. The differences in cost function , asymmetry parameter and phase function (Figs. 4c and f and 5a) between the habit combinations with lowest cost function values and asymmetry parameter between the best habit combinations are very small, but the relative differences in β and ξ are somewhat larger (Fig. 5b). This which makes the choice of a single "best" habit combination for representing the SSPs of snow somewhat arbitrary. For further use in representing the SSPs as a function of wavelength and size, we select the following habit combination: 36 % of SR droxtals, 26 % of aggregates of 10 SR plates, and 38 % strongly distorted 2nd generation Koch fractals ($t = 0.50$), where the weights refer to fractional contributions to the projected area. For this habit combination, the cost function is 0.086, g=0.778, and ξ=1.62. This habit combination is represented with a blue line in Fig. 4c and f and is marked with an arrow in Fig. 5a and b. Hereafter, this habit combination will be referred to as the "optimized habit combination" (OHC). The primary reason why we selected this OHC rather than either of the first two habit combinations in Table 1, which have a marginally

lower cost function, is that these habit combinations include either hollow columns or bullet rosettes. For these habits (unlike aggregates of plates), the particle geometry assumed in the Yang et al. (2013) database depends on particle size, with the aspect ratio of the crystals increasing with their length. However, due to snow metamorphosis on ground, size-shape relationships based on crystal growth in ice clouds are most likely not valid for snow. Therefore, we considered it better to use a crystal geometry that is independent of size. This also helps to keep the SSP parameterization simpler.

5 Snow single-scattering properties as a function of size and wavelength

The SSPs, including the extinction efficiency Q_{ext}, single-scattering co-albedo β, asymmetry parameter g and scattering phase function $P_{11}(\theta_s)$ were determined for the OHC, for 140 wavelengths between 0.199 and 3 µm and for 48 particle sizes between 10 and 2000 µm. Here, the size is defined as the volume-to-projected area equivalent radius $r_{\text{vp}} = 0.75V/P$. As stated above, the OHC consists of SR droxtals, aggregates of 10 SR plates, and strongly distorted Koch fractals. The SSPs for droxtals and aggregates of plates were taken from the Yang et al. (2013) database (interpolated to fixed values of r_{vp}) while those of Koch fractals were computed using the geometric optics code of Macke (1993), as explained in Sect. 2. Four caveats should be noted:

1. due to problems associated with the truncation of numerical results to a finite number of digits (P. Yang, personal communication, 2013), the values of β in the Yang et al. (2013) database are unreliable in cases of very weak absorption. To circumvent this issue, it was assumed that in cases of weak absorption ($\beta < 0.001$ for Koch fractals), the values for droxtals and aggregates of plates may be approximated as

$$\beta_{\text{droxtal}}(\lambda, r_{\text{vp}}) = 0.943\beta_{\text{fractal}}(\lambda, r_{\text{vp}}), \tag{6}$$

$$\beta_{\text{aggregate}}(\lambda, r_{\text{vp}}) = 0.932\beta_{\text{fractal}}(\lambda, r_{\text{vp}}). \tag{7}$$

Here the scaling factors were determined as $\overline{\beta_{\text{droxtal}}}/\overline{\beta_{\text{fractal}}}$ and $\overline{\beta_{\text{aggregate}}}/\overline{\beta_{\text{fractal}}}$, where the overbar refers to averages over the cases in which $0.001 < \beta_{\text{fractal}} < 0.01$ and the size parameter $x = 2\pi r_{\text{vp}}/\lambda > 100$.

2. While the largest maximum dimension for particles in the Yang et al. (2013) database is 10 000 µm for all habits, the corresponding maximum values of r_{vp} are smaller and depend on the habit. For droxtals, $r_{\text{vp,max}} = 4218\,\mu\text{m}$, while for the aggregates of 10 plates, it is only $r_{\text{vp,max}} = 653\,\mu\text{m}$. Thus, to extend the SSPs for the OHC to sizes up to $r_{\text{vp}} = 2000\,\mu\text{m}$, we extrapolated the SSPs for the aggregates of plates based on how the SSPs depend on size for Koch fractals. See Appendix A for details.

3. The SSPs for Koch fractals were computed using a geometric optics code, which means that the accuracy deteriorates somewhat in cases with smaller size parameters (typically for $x < 100$). This issue pertains mainly to small snow ~~crystals~~ grains at near-IR wavelengths (e.g., for $\lambda = 2.5\,\mu\text{m}$, $x = 100$ corresponds to $r_{\text{vp}} \approx 40\,\mu\text{m}$).

4. Lastly but importantly, since the OHC was selected based on measurements at a single wavelength $\lambda = 0.80\,\mu\text{m}$ for only two cases, there is no guarantee that it represents the snow SSPs equally well at other wavelengths, or for all snow grain sizes.

Figure 6 compares wavelength-dependent SSPs for the OHC with those for two shape assumptions previously used in modeling snow optics: spheres and Koch fractals (distorted Koch fractals with $t = 0.18$ were selected for this comparison; this is close though not identical to the shape assumption used by Kokhanovsky et al., 2011). Two monodisperse cases are considered, with $r_{\text{vp}} = 50\,\mu\text{m}$ and $r_{\text{vp}} = 1000\,\mu\text{m}$, respectively. For all three habits, the asymmetry parameter g (Fig. 6a) and the single-scattering co-albedo β (Fig. 6b) show well-known dependencies on particle size and wavelength. Thus, g is largely independent of both λ and r_{vp} in the visible region where β is very small. In the near-IR region, β increases with increasing imaginary part m_i of the refractive index and with increasing particle size. With increasing β, the fractional contribution of diffraction to the phase function increases, which results in larger values of g (e.g. Macke et al., 1996) . The most striking differences between

the three shape assumptions occur for the asymmetry parameter, especially in the visible region, where $g \approx 0.89$ for spheres, $g \approx 0.74$ for distorted Koch fractals, and $g \approx 0.77$–0.78 for the OHC. The values of β for the OHC are also intermediate between the two single-shape cases: larger than those for spheres (except for $r_{\mathrm{vp}} = 1000\,\mu\mathrm{m}$ at the strongly absorbing wavelengths $\lambda > 1.4\,\mu\mathrm{m}$), but slightly smaller than those for distorted Koch fractals. The implications of these differences for snow albedo are considered in Sect. 7.

~~As~~ While the co-albedo values in Fig. 6b are strongly wavelength dependent through m_i, ~~we consider in Fig. 6c the~~ the effects of shape on absorption can be distinguished more clearly by considering the non-dimensional absorption ~~parameter~~ parameter (Kokhanovsky and Zege, 2004; Kokhanovsky, 2013)

$$\xi = \frac{C_{\mathrm{abs}}}{\gamma V} = \frac{Q_{\mathrm{ext}} P \beta}{\gamma V}, \tag{8}$$

where C_{abs} is the absorption cross section, Q_{ext} the extinction efficiency, P the projected area and V the particle volume, and $\gamma = 4\pi m_i/\lambda$, m_i being the imaginary part of ice refractive index. Figure 6c displays ξ ~~(defined by Eq. (8) above), to show more clearly the shape effects on absorption~~ at the wavelengths $\lambda = 0.199$–$1.4\,\mu\mathrm{m}$, where absorption by snow is relatively weak. Consistent with the co-albedo values (Fig. 6b) and previous studies ~~(e.g. ?)~~ (e.g. Kokhanovsky and Nauss, 2005), Fig. 6c indicates that absorption is generally stronger for non-spherical than spherical particles, for the same r_{vp}. The difference is particularly clear in the visible region, where $\xi \leq 1.3$ for spheres (except for some spikes that occur in the Mie solution especially for $r_{\mathrm{vp}} = 50\,\mu\mathrm{m}$), ≈ 1.7 for the Koch fractals, and slightly over 1.6 for the OHC.

At wavelengths beyond $\lambda = 1.0\,\mu\mathrm{m}$, ξ tends to decrease especially for the larger particle size $r_{\mathrm{vp}} = 1000\,\mu\mathrm{m}$ considered, as absorption no longer increases linearly with m_i. Furthermore, in the UV region, Koch fractals and the OHC show a distinct increase in ξ with decreasing wavelength. This is related to the corresponding increase of the real part of the refractive index m_{r}. Interestingly, it is found that for these shape assumptions, absorption scales linearly with m_{r}^2, and furthermore, for Koch fractals, $\xi/m_{\mathrm{r}}^2 \approx 1$ when absorp-

tion is weak (Fig. 6d). For spheres, the dependence of ξ on m_r is weaker. Equation (4) in Bohren and Nevitt (1983) provides the absorption efficiency of weakly absorbing spheres in the limit of geometric optics, which can be rewritten in terms of ξ as

$$\xi = \frac{m_\mathrm{r}^3 - \left(m_\mathrm{r}^2 - 1\right)^{3/2}}{m_\mathrm{r}} = m_\mathrm{r}^2 - \frac{\left(m_\mathrm{r}^2 - 1\right)^{3/2}}{m_\mathrm{r}}. \quad (9)$$

For $r_\mathrm{vp} = 1000\,\mu\mathrm{m}$, ξ for spheres follows this approximation closely until $\lambda \approx 1.0\,\mu\mathrm{m}$ (Fig. 6c and d). However, it appears that for Koch fractals, only the first term should be included.

It should be noted that ξ for the OHC is not independent of that for Koch fractals (due to the scaling of co-albedo in Eqs. (6) and (7)). However, we found that ξ also scales linearly with m_r^2 for Gaussian spheres (this was tested for $\sigma = 0.17$, $\nu = 2.9$, $l_\mathrm{max} = 15$), suggesting that this might apply more generally to complex non-spherical particles.

Finally, it should be recalled that our choice of the OHC was based on phase function observations at the wavelength $\lambda = 0.80\,\mu\mathrm{m}$. At this wavelength, absorption is so weak that it has very little impact on the phase function. Therefore, these observations cannot be used to constrain absorption by snow. In spite of this, we think it is worth providing a co-albedo parameterization based on the OHC (Eq. 11 in Sect. 6.2). The reason for this is that snow grains are distinctly non-spherical, and for non-spherical particles, ξ and β are, in general, systematically larger than those for spheres, as demonstrated by Fig. 6. In fact, considering the wavelength $\lambda = 0.80\,\mu\mathrm{m}$, the values of ξ integrated over the size distribution defined by Eq. (3) are, for the large majority of the non-spherical shapes considered, between 1.55 and 1.75, the value for the OHC being $\xi = 1.62$ (Table 1). The corresponding value for spheres is substantially lower, $\xi = 1.29$. Thus, while we cannot constrain ξ or β precisely, it is very likely that the actual values for snow exceed those for spheres.

6 Parameterizations for the single-scattering properties of snow

In this section, parameterization equations are provided for the computation of snow SSPs (extinction efficiency Q_ext, single-scattering co-albedo β, asymmetry parameter g and scat-

tering phase function $P_{11}(\theta_s)$) for the OHC discussed above. The parameterizations are provided for the size range $r_{vp} = 10$–$2000\,\mu m$ and wavelength range $\lambda = 0.199$–$2.70\,\mu m$. They are expressed in terms of the size parameter x and real and imaginary parts of refractive index (m_r and m_i). Here, the size parameter defined with respect to the volume-to-projected area equivalent radius is used:

$$x = x_{vp} = 2\pi \frac{r_{vp}}{\lambda}. \tag{10}$$

For the OHC, the size parameter defined with respect to the projected area is $x_p \approx 1.535 x_{vp}$.

6.1 Extinction efficiency

The extinction efficiency Q_{ext} for the OHC is displayed in Fig. 7. For most of the wavelength and size region considered, Q_{ext} is within 1 % of the asymptotic value $Q_{ext} = 2$ for particles large compared to the wavelength. Note that the deviations from $Q_{ext} = 2$ are probably somewhat underestimated because the OHC includes Koch fractals, for which $Q_{ext} \equiv 2$ due to the use of geometric optics. For simplicity, we assume this value in our parameterization, while acknowledging that the actual value tends to be slightly higher especially for small snow grains in the near-IR region.

6.2 Single-scattering co-albedo

The single scattering co-albedo is parameterized as

$$\beta = 0.470 \left\{ 1 - \exp\left[-2.69 x_{abs} \left(1 - 0.31 \min\left(x_{abs}, 2 \right)^{0.67} \right) \right] \right\}, \tag{11}$$

where the size parameter for absorption is defined as

$$x_{abs} = \frac{2\pi r_{vp}}{\lambda} m_i m_r^2. \tag{12}$$

The general form of this parameterization was inspired by the ice crystal optics parameterization of van Diedenhoven et al. (2014); however our definition of x_{abs} differs from theirs

in that the factor m_r^2 is included, based on the findings of Fig. 6c and d. The performance of this parameterization is evaluated in Fig. 8a and c. In Fig. 8a, the parameterized values (shown with contours) follow extremely well the reference values computed for the OHC (shading). The relative errors $\Delta\beta/\beta$ are mostly below 1 %; errors larger than 3 % (and locally even > 10 %) occurring only for small snow ~~crystals~~ grains ($r_{vp} < 50\,\mu m$) at wavelengths $\lambda > 1.2\,\mu m$. The rms value of the relative errors (computed over 125 values of $\lambda \in [0.199, 2.7\,\mu m]$ and 48 roughly logarithmically spaced values of $r_{vp} \in [10, 2000\,\mu m]$) is 1.4 %.

6.3 Asymmetry parameter

The asymmetry parameter is parameterized as

$$g = 1 - 1.146[m_r - 1]^{0.8}[0.52 - \beta]^{1.05}\left[1 + 8x_{vp}^{-1.5}\right], \quad (13)$$

where the parameter values were determined by trial and error, with the aim of minimizing the rms error in g. The form of this ~~parametrization~~ parameterization reflects how g decreases with increasing m_r, increases with increasing absorption (i.e., increasing co-albedo β), and increases slightly with increasing size parameter x_{vp} even at non-absorbing wavelengths~~(in the size parameter region where the geometric optics is not yet fully valid)~~, in part because the diffraction peak becomes narrower. In practice, the co-albedo β plays the most important role (cf. van Diedenhoven et al., 2014), which explains the general increase of g with increasing r_{vp} in the near-IR region (Fig. 8b). The parameterized values of g (shown with contours in Fig. 8b) follow the reference values (shading) very well. Note that when producing these results, parameterized rather than exact β was used in Eq. (13). The differences from the reference are mostly below 0.001 at the weakly absorbing wavelengths up to $\lambda = 1.4\,\mu m$, and while larger differences up to $|g| = 0.007$ occur at the strongly absorbing wavelengths (Fig. 8d), the overall rms error is only 0.0019.

6.4 Phase function

The phase function parameterization consists of three terms,

$$P_{11}(\theta_s) = w_{\text{diff}} P_{\text{diff}}(\theta_s) + w_{\text{ray}} P_{\text{ray}}(\theta_s) + P_{\text{resid}}(\theta_s), \tag{14}$$

which represent contributions due to diffraction, due to the ray tracing part, and a residual that corrects for errors made in approximating the former two parts. The weight factors for diffraction w_{diff} and ray tracing w_{ray} are given by

$$w_{\text{diff}} = \frac{1}{Q_{\text{ext}}\omega} \approx \frac{1}{2\omega}, \tag{15}$$

$$w_{\text{ray}} = \frac{Q_{\text{ext}}\omega - 1}{Q_{\text{ext}}\omega} \approx \frac{2\omega - 1}{2\omega}, \tag{16}$$

where the latter form assumes $Q_{\text{ext}} = 2$ (e.g. Macke et al., 1996) .

It should be noted that in practice, the division of the phase function expressed by Eq. (14) is conceptual rather than rigorous. The fitting was based on the total phase function rather than the diffraction and ray tracing parts separately, as these two parts are not separated in the Yang et al. (2013) database. The general aim of the fitting was to minimize the rms errors in $\ln P_{11}$.

For diffraction, the HG phase function (Henyey and Greenstein, 1941) is used:

$$P_{\text{diff}}(\theta_s) = P_{\text{HG}}(g_{\text{diff}}, \theta_s). \tag{17}$$

The HG phase function is given by

$$P_{\text{HG}}(g, \theta_s) = \frac{1 - g^2}{[1 + g^2 - 2g\cos\theta_s]^{3/2}}, \tag{18}$$

and the asymmetry parameter g_{diff} is approximated as

$$g_{\text{diff}} = 1 - 0.60/x_{\text{vp}} = 1 - 0.921/x_{\text{p}}, \tag{19}$$

This treatment of diffraction, including the parameterization where we have utilized the relation $x_p \approx 1.535 x_{\mathrm{vp}}$ specific to the OHC. Compared to the parameterization derived by van Diedenhoven et al. (2014) , Eq. (19) yields somewhat lower values of g_{diff}, which to some extent compensates for the fact that the actual shape of the diffraction peak deviates from the HG phase function. Overall, this treatment of diffraction is a rough approximation, and clearly not ideal for studies of very near-forward scattering, but it serves well the current purpose. On one hand, it improves the accuracy compared to the assumption of a delta spike, and on the other hand, the HG phase function has a very simple Legendre expansion

$$P_{\mathrm{HG}}(g, \theta_{\mathrm{s}}) = \sum_{n=0}^{\infty} (2n+1) g^n P_n(\cos\theta_{\mathrm{s}}), \tag{20}$$

where P_n denotes the nth order Legendre polynomial. This facilitates greatly the use of P_{HG} in radiative transfer models such as DISORT (Stamnes et al., 1988).

The phase function for the ray tracing part is approximated as

$$P_{\mathrm{ray}}(\theta_{\mathrm{s}}) = w_1 P_{\mathrm{HG}}(g_1, \theta_{\mathrm{s}}) + (1 - w_1), \tag{21}$$

where the latter term $1 - w_1$ is intended to emulate the nearly flat behaviour of P_{11} in the near-backward scattering directions. The weight factor for the HG part is parameterized as

$$w_1 = 1 - 1.53 \cdot \max(0.77 - g_{\mathrm{ray}}, 0)^{1.2}, \tag{22}$$

where g_{ray} is the asymmetry parameter for the ray tracing (i.e., non-diffraction) part. It is derived from the condition $g = w_{\mathrm{diff}} g_{\mathrm{diff}} + w_{\mathrm{ray}} g_{\mathrm{ray}}$, which yields

$$g_{\mathrm{ray}} = \frac{g - w_{\mathrm{diff}} g_{\mathrm{diff}}}{w_{\mathrm{ray}}}. \tag{23}$$

The total asymmetry parameter g is computed using Eq. (13) above. Finally, the asymmetry parameter g_1 needed in Eq. (21) is

$$g_1 = g_{\mathrm{ray}} / w_1. \tag{24}$$

While the sum of the first two terms of Eq. (14) already provides a reasonably good approximation of the phase function (see below), the ~~accuracy~~ fit can be further improved by introducing the residual P_{resid}, which is represented as a Legendre series. It turns out that, except for cases with strong absorption, a series including terms only up to $n = 6$ yields very good results

$$P_{\text{resid}}(\theta_s) = \sum_{n=0}^{6} (2n+1) a_n P_n(\cos\theta_s), \tag{25}$$

provided that δ-M-scaling (Wiscombe, 1977) is applied, with a truncated fraction $f = a_6$. Thus,

$$\begin{aligned} P_{\text{resid}}(\theta_s) \approx P^*_{\text{resid}}(\theta_s) &= 2f\delta(1-\cos\theta_s) + (1-f)\sum_{n=0}^{5}(2n+1)\frac{a_n - f}{1-f} P_n(\cos\theta_s) \\ &= 2a_6\delta(1-\cos\theta_s) + \sum_{n=0}^{5}(2n+1)(a_n - a_6) P_n(\cos\theta_s), \end{aligned} \tag{26}$$

where δ is Dirac's delta function. What remains to be parameterized, then, are the coefficients $a_0 \ldots a_6$. A rough but useful approximation is to express them as a simple function of the co-albedo β and the asymmetry parameter g:

$$a_n = c_{1n} + c_{2n}\beta + c_{3n}g + c_{4n}\beta g. \tag{27}$$

The parameterization coefficients c_{mn} were determined by minimizing the rms errors of a_n with the LAPACK subroutine DGELS, and they are given in Table 2. Note specifically that the coefficients c_{m0} and c_{m1} are all zero. The formulation of P_{diff} and P_{ray} ensures that the phase function (Eq. 14) is correctly normalized and that its asymmetry parameter is consistent with Eq. (13) even without considering P_{resid}; therefore $a_0 = a_1 = 0$. Equivalently,

the Legendre expansion may be replaced by an ordinary polynomial. This yields

$$P_{\text{resid}}(\theta_s) \approx P^*_{\text{resid}}(\theta_s) = 2a_6\delta(1-\cos\theta_s) + \sum_{n=0}^{5} b_n(\cos\theta_s)^n, \tag{28}$$

where

$$b_n = d_{1n} + d_{2n}\beta + d_{3n}g + d_{4n}\beta g. \tag{29}$$

~~The~~ Here, the coefficients d_{mn} were obtained directly based on the coefficients c_{mn} in Eq. (27), by writing out the Legendre polynomials in Eq. (26). Their numerical values are given in Table 3. In summary, the phase function parameterization reads

$$P_{11}(\theta_s) = w_{\text{diff}}P_{\text{HG}}(g_{\text{diff}},\theta_s) + w_{\text{ray}}w_1P_{\text{HG}}(g_1,\theta_s) + w_{\text{ray}}(1-w_1) + P_{\text{resid}}(\theta_s), \tag{30}$$

where $P_{\text{resid}}(\theta_s)$ is given by Eq. (26) or, equivalently, by Eq. (28).

Finally, it is worth noting how this parameterization can be used in DISORT, when applying a "δ-NSTR-stream" approximation for radiative transfer, NSTR being the number of streams. In this case, DISORT assumes by default a truncation factor $f = a_{\text{NSTR}}$. If NSTR > 6, the Legendre expansion for P_{resid} in Eq. (26) should be formally extended to $n = \text{NSTR}$, with $a_n = a_6$ for $n = 7 \ldots \text{NSTR}$. Thus the Legendre coefficients input to DISORT become

$$p_n = \begin{cases} 1, & \text{for } n = 0 \\ w_{\text{diff}}g_{\text{diff}}^n + w_{\text{ray}}w_1g_1^n + a_n, & \text{for } 1 \le n \le 6 \\ w_{\text{diff}}g_{\text{diff}}^n + w_{\text{ray}}w_1g_1^n + a_6, & \text{for } 7 \le n \le \text{NSTR} \end{cases}, \tag{31}$$

where we have utilized the Legendre expansion of the HG phase function in Eq. (20).

To provide a compact view of how the phase function parameterization performs, we define, analogously to Eq. (4), a cost function as the rms error of the natural logarithm of

the phase function,

$$\text{cost} = \sqrt{\frac{\int_{0^\circ}^{180^\circ} \left(\ln P_{11}^{\text{param}} - \ln P_{11}^{\text{OHC}}\right)^2 \sin\theta_s \mathrm{d}\theta_s}{\int_{0^\circ}^{180^\circ} \sin\theta_s \mathrm{d}\theta_s}}, \tag{32}$$

where P_{11}^{param} is the parameterized phase function and P_{11}^{OHC} is the reference value, defined here as the "exact" phase function computed for the OHC. Figure 9a shows the cost function for the full phase function parameterization, and Fig. 9b for a simpler parameterization that includes only the first two terms of Eq. (14) (i.e., P_{resid} is excluded). Note that the parameterized phase function is computed here using parameterized (rather than exact) values of Q_{ext}, β, and g.

Most importantly, Fig. 9a shows that in a large part of the wavelength and size domain, the accuracy of the full parameterization is very high, with cost function values ≤ 0.03. This corresponds to a typical relative accuracy of 3 % in the computed phase function, as compared with the reference values for the OHC. The primary exception is that substantially larger errors occur for large snow ~~crystals~~ grains at the strongly absorbing wavelengths in the near-IR region. In broad terms, the accuracy starts to degrade appreciably when $\beta > 0.3$, that is, in cases in which snow reflectance is quite low ($\beta = 0.3$ corresponds roughly to a spherical albedo of 0.03 for an optically thick snow layer). At the largest wavelengths considered ($\lambda > 2.5\,\mu\text{m}$), somewhat larger values of the cost function also occur for smaller values of r_{vp} and β. The cost function for the simplified parameterization (Fig. 9b) shows mainly the same qualitative features as the full parameterization in Fig. 9a; however, the cost function values in the weakly absorbing cases are ≈ 0.07, in contrast with the values of ≈ 0.03 for the full parameterization.

Figure 10 displays examples of phase function for nine combinations of λ and r_{vp}. In the weakly absorbing cases in Fig. 10a–c, and also at the more strongly absorbing wavelength $\lambda = 1.50\,\mu\text{m}$ for $r_{\text{vp}} = 10\,\mu\text{m}$ and $r_{\text{vp}} = 100\,\mu\text{m}$ (Fig. 10d, e), the full parameterization follows extremely well the reference phase function computed for the OHC, to the extent that the curves are almost indistinguishable from each other. Even at $\lambda = 2.00\,\mu\text{m}$, the deviations from the reference are generally small in the cases with relatively small snow ~~crystals~~

grains ($r_{vp} = 10\,\mu m$ and $r_{vp} = 100\,\mu m$; Fig. 10g, h), although backward scattering is slightly overestimated in the latter case. In contrast, in cases with very strong absorption and large snow ~~crystals~~ grains ($r_{vp} = 1000\,\mu m$ for $\lambda = 1.50\,\mu m$ and $\lambda = 2.00\,\mu m$ in Fig. 10f, i) there are more substantial deviations from the reference. Here, the parameterized phase function is generally underestimated in the backscattering hemisphere and overestimated at $\theta_s < 30°$ especially for $\lambda = 2.00\,\mu m$; $r_{vp} = 1000\,\mu m$. Furthermore, the Legendre expansion in P_{resid} leads to oscillations in the backscattering hemisphere, which do not occur in the reference phase function. Again, it should be noted that the largest errors occur in cases in which snow is very "dark": the spherical albedo corresponding to the cases in Fig. 10f and i is only ~ 0.005.

In many respects, the simplified parameterization (i.e., without P_{resid}) produces quite similar phase functions as the full parameterization. Two differences can be noted. First, the simplified parameterization does not capture the slight increase in phase function at angles larger than $\theta_s \approx 120$–$130°$, which is present in the reference and full parameterization phase functions, and which was also suggested by the CLIMSLIP data for blowing snow at $\lambda = 0.80\,\mu m$, along with the other phase functions in Fig. 1b. Second, in the cases with very strong absorption (Fig. 10f and i) the simplified phase function avoids the oscillations seen in the full parameterization.

The utility of providing a phase function parameterization is further demonstrated by showing in Fig. 10, for comparison, the HG phase function computed using the asymmetry parameter from Eq. (13). The differences from the reference phase function are systematic. The scattering in the diffraction peak is underestimated (although this is not properly seen from Fig. 10), but otherwise forward scattering is overestimated until a scattering angle of $\approx$35°–80°, depending on the case. Conversely, at sideward and backscattering angles, scattering is underestimated. Consequently, the cost function values for the HG phase function given in Fig. 10 substantially exceed those for both the full and simplified phase function parameterizations.

7 Radiative transfer applications

In this section, we consider the impact of snow optics assumptions on snow spectral albedo A and reflected radiances $L^{\uparrow}$.The purpose is, on one hand, to evaluate the accuracy of the proposed snow SSP parameterization, and on the other hand, to compare the results obtained with three shape assumptions: spheres, 2nd generation Koch fractals (distorted with $t = 0.18$) and the OHC proposed here. Throughout this section, the results for the OHC are used as the reference, although it is clear that they cannot be considered an absolute benchmark for scattering by snow. The radiative transfer computations were performed with DISORT (with 32 streams, delta-M-scaling included), assuming an optically thick (i.e., semi-infinite) layer of pure snow with a monodisperse size distribution.

Like most other solar radiative transfer studies involving snow, close-packed effects are ignored in the calculations. It has been shown by Kokhanovsky (1998) that, at least as a first approximation, they do not have a pronounced impact on the snow reflectance.

First, snow albedo as a function of λ and r_{vp} is considered in Fig. 11. Direct incident radiation with a cosine of zenith angle $\mu_0 = \cos\theta_0 = 0.5$ is assumed. Figure 11a demonstrates the well-known features of snow albedo: the values are very high in the UV and visible region, and decrease with increasing particle size in the near-IR. The results computed using the parameterized snow optical properties Q_{ext}, β, g, and P_{11} are almost indistinguishable from those obtained using the "exact" optical properties for the OHC. The differences between these two are mostly within 0.002 (Fig. 11b), although larger differences up to 0.02 occur for very small snow grains ($r_{\text{vp}} \approx$10–20 µm) at wavelengths with strong absorption by snow ($\lambda > 1.4$ µm). These results are only weakly sensitive to the assumed direction of incident radiation. Furthermore, while the parameterized albedo values were computed using the full phase function parameterization, the values for the simplified parameterization (without P_{resid} in Eq. (14)) differed very little from them, mostly by less than 0.001.

For distorted Koch fractals, the albedo values are higher than those for the OHC, but the difference is rather small, at most 0.017 (Fig. 11c). Conversely, for spheres, the albedo values are lower, with largest negative differences of -0.08 ~~to~~ from the reference (Fig. 11d).

This stems from the higher asymmetry parameter of spheres, which is only partly compensated by their lower co-albedo (Fig. 6). To put it in another way, for a given albedo A in the near-IR region, a smaller (slightly larger) particle size is required for spheres (for distorted Koch fractals) than for the OHC.

To compare the simulated radiance distributions to the reference, we next consider the root-mean-square error in the logarithm of reflected radiances integrated over the hemisphere:

$$\text{LOGRMSE} = \sqrt{\frac{1}{2\pi}\int_0^{2\pi}\int_0^{\pi/2}\left[\ln L^{\uparrow}(\theta,\phi) - \ln L^{\uparrow}_{\text{OHC}}(\theta,\phi)\right]^2 \sin\theta \mathrm{d}\theta\mathrm{d}\phi}, \tag{33}$$

where θ and ϕ denote the zenith angle and azimuth angle, respectively, and $L^{\uparrow}_{\text{OHC}}$ is the radiance in the reference computations for the OHC. Figure 12a–c shows LOGRMSE as a function of particle size and wavelength for the full parameterization, for three directions of incident radiation ($\mu_0 = 0.8$, $\mu_0 = 0.4$ and $\mu_0 = 0.1$, corresponding to $\theta_0 = 36.9°$, $\theta_0 = 66.4°$ and $\theta_0 = 84.3°$, respectively). For weakly absorbing wavelengths up to $\lambda = 1.4\,\mu\text{m}$, the performance of the parameterization is extremely good for all particle sizes, with values of LOGRMSE < 0.01 for $\mu_0 = 0.8$ and $\mu_0 = 0.4$ and between 0.01 and 0.02 for $\mu_0 = 0.1$. LOGRMSE ~ 0.01 implies a typical relative accuracy of $\sim 1\,\%$ in the reflected radiances. The accuracy in radiances at weakly absorbing wavelengths is even higher than that in the phase function (Fig. 9a) because strong multiple scattering diminishes the effect of phase function errors. At wavelengths $\lambda > 1.4\,\mu\text{m}$, LOGRMSE increases, not only due to larger phase function errors, but also because multiple scattering is reduced due to stronger absorption. Even here, LOGRMSE stays mainly below 0.05 for relatively small snow grains ($r_{\text{vp}} < 100\,\mu\text{m}$), but substantially larger errors occur in the cases with large and strongly absorbing grains, consistent with the modest accuracy of the phase function parameterization in these cases (Fig. 9b). These errors depend only weakly on μ_0. It should be noted that the largest relative errors occur in cases where the reflected radiances and radiance errors are small in an absolute sense and probably matter little for practical applications.

Values of LOGRMSE obtained using the simplified phase function parameterization are shown in Fig. 12d–f. Consistent with the phase function errors (cf. Fig. 9a vs. b), the simplified parameterization is slightly less accurate in simulating reflected radiances than the full parameterization, except for the most strongly absorbing cases. Nevertheless, the accuracy is quite high for the weakly absorbing cases; LOGRMSE ranging from ~ 0.01 (or even less) for $\mu_0 = 0.8$ to ~ 0.03 for $\mu_0 = 0.1$.

For comparison, Fig. 12g and h shows LOGRMSE computed for distorted Koch fractals and spheres (for $\mu_0 = 0.4$ only). Unsurprisingly, LOGRMSE is generally smaller for Koch fractals than for spheres (e.g., 0.05–0.10 in weakly absorbing cases, as compared with ~ 0.20 for spheres). In both cases, again excepting large particles at strongly absorbing wavelengths, the values of LOGRMSE are substantially larger than those associated with the snow SSP parameterization. This indicates that in general, ~~the inaccuracy~~ numerical fitting errors in the parameterization ~~is~~ are a minor issue in comparison with the radiance differences associated with different shape assumptions.

Examples of the angular distribution of reflected radiances are given in Figs. 13 and 14. Here, only a single particle size $r_{\text{vp}} = 200\,\mu\text{m}$ is considered, and the azimuth angle for incident radiation is $\phi_0 = 0°$. In Fig. 13, results are shown for three zenith angles of incident radiation, corresponding to $\mu_0 = 0.8$, $\mu_0 = 0.4$, and $\mu_0 = 0.1$, for a single wavelength $\lambda = 0.80\,\mu\text{m}$. In Fig. 14, three wavelengths are considered ($\lambda = 0.30$, 1.40 ~~, and 2.00~~and 2.20 µm) but for $\mu_0 = 0.4$ only. In each figure, panels (a)–(c) display the distribution of reflected radiances in the reference calculations for the OHC, while the remaining panels show the relative differences from the reference for distorted Koch fractals with $t = 0.18$ (panels d–f), for spheres (g–i), for the Henyey-Greenstein phase function (j–l), for the full snow SSP parameterization (~~j–l~~m–o), and for the simpler parameterization without P_{resid} in Eq. (14) (~~m–o~~p–r). For brevity, only some main points are discussed.

First, it is seen, consistent with Fig. 12, that in general, the radiance distribution for spheres differs more from the reference than the distribution for Koch fractals does. For example, for $\lambda = 0.80\,\mu\text{m}$ and $\mu_0 = 0.4$, both positive and negative differences larger than 50 % occur for spheres (Fig. 13h), while for Koch fractals, the differences exceed 10 % only

locally (Fig. 13e). Furthermore, in the same case, the radiance errors are ~~< 2~~< 1 % almost throughout the (θ, ϕ) domain for the full parameterization (Fig. 13~~k~~n), and mostly < 2 % even for the simplified parameterization (Fig. 13~~n~~q). In contrast, when the HG phase function is employed in the calculations, the differences from the reference reach locally 30 % and −40 % (Fig. 13k).

Second, while the results noted above for $\lambda = 0.80$ µm and $\mu_0 = 0.4$ are also mostly valid for $\mu_0 = 0.8$ and $\mu_0 = 0.1$, and for ~~$\lambda = 0.30$ and~~ $\lambda = 0.30$, 1.40 and 2.20 µm, some quantitative differences can be noted. When μ_0 decreases from 0.8 to 0.1, the pattern of reflected radiances becomes increasingly non-uniform and more sensitive to both the assumed particle shape and the errors in phase function parameterization. This occurs because the relative role of first-order scattering increases (e.g., Mischenko et al., 1999). For the same reason, the sensitivity of the radiance pattern to the phase function increases with increasing absorption. Thus, while the qualitative features are ~~similar at the weakly absorbing wavelengths~~ mostly similar at all wavelength considered here, the relative differences are generally larger at $\lambda = $ ~~0.30~~1.40 µm and $\lambda = $ ~~0.80~~2.20 µm ~~and at the moderately absorbing wavelength~~ than at $\lambda = $ ~~1.40~~0.30 µm ~~, the relative differences are generally largest at~~ and $\lambda = $ ~~1.40~~0.80 µm. ~~At the strongly absorbing~~ Especially at the wavelength $\lambda = $ ~~2.00~~2.20 µm, at which snow absorption is quite strong and the albedo for the OHC is only ~~0.011~~0.11, the radiance pattern is ~~determined entirely~~ dominated by first-order scattering and is thus very sensitive to the details of the phase function. In a relative (though not absolute) sense, the errors in parameterized radiances are ~~much~~ also somewhat larger than at the other wavelengths considered ~~, in part due to larger errors in the phase function (cf.~~ (Fig. ~~9~~14o and r).

Third, even at weakly absorbing wavelengths, the role of first-order scattering is clearly discernible: many differences in the pattern of reflected radiances can be traced directly to phase function differences. For example, ~~at~~ considering the results for $\lambda = 0.80$ µm ~~, three~~ for both $\mu_0 = 0.4$ and $\mu_0 = 0.1$, we note the following:

- Three regions appear in the radiance differences between distorted Koch fractals and the OHC ~~for both $\mu_0 = 0.4$ and $\mu_0 = 0.1$ (~~in Fig. 13e and f~~)~~. Going from left to right, neg-

ative radiance differences occur at large values of θ and small values of ϕ (roughly for $\theta > 65°$ and $\phi < 20°$), followed by a region of positive differences, and another region of negative differences (roughly for $\theta > 40°, \phi > 140°$). These regions occur because the phase function for Koch fractals is larger than that for the OHC at intermediate scattering angles ($29° \leq \theta_s \leq 134°$) but smaller in the near-forward and near-backward directions.

– For spheres in Fig. 13h and i, the reflected radiances greatly exceed those for the OHC for roughly $\theta > 60°, \phi < 40°$ because the phase function for spheres is generally larger than that for the OHC for $\theta_s < 54°$. Conversely, at larger θ_s, the phase function for spheres is (mostly) considerably smaller than that for the OHC. This results in generally smaller reflected radiances for spheres in most of the (θ,ϕ) domain with $\phi > 50°$. As an exception, the icebow feature for spheres at $\theta_s \approx 135°$ results in an arc with larger radiances for spheres than for the OHC.

– For the HG phase function, the pattern of overestimated radiances up to $\phi \sim 60°$ and underestimated radiances at larger azimuth angles (Fig. 13k and l) arises because the HG phase function exceeds that for the OHC for $\theta_s < 80°$ and falls below it at larger scattering angles (see also Fig. 10).

8 Summary

In this work, measurements of angular distribution of scattering by blowing snow made during the CLIMSLIP campaign in Svalbard were used to select a shape model for representing the single-scattering properties (SSPs) of snow. An optimized habit combination (OHC) consisting of severely rough (SR) droxtals, aggregates of SR plates and strongly distorted Koch fractals was selected. The SSPs (extinction efficiency Q_{ext}, single-scattering co-albedo β, asymmetry parameter g and phase function P_{11}) were then computed for the OHC as a function of wavelength and snow grain size. Furthermore, parameterization equations were developed for the SSPs for the wavelength range $\lambda = 0.199$–$2.7\,\mu m$, and

for snow grain volume-to-projected area equivalent radii r_{vp} = 10–2000 µm. The parameterizations are expressed in terms of the size parameter and real and imaginary parts of refractive index. The relative accuracy of the parameterization, as compared with the reference calculations for the OHC, is very high for the single-scattering co-albedo and the asymmetry parameter. This is also true for the phase function parameterization in weakly and moderately absorbing cases, while in strongly absorbing cases (mainly for $\beta > 0.3$), the accuracy deteriorates. Such strongly absorbing cases are, however, associated with small values of snow albedo and reflected radiances.

The SSPs and the resulting snow albedo and reflected radiances for the OHC were compared with two previously used shape assumptions for snow grains, spheres and second-generation Koch fractals. The asymmetry parameter for the OHC is distinctly smaller than that for spheres but slightly higher than that for Koch fractals. Consistent with this, snow albedo for the OHC is generally substantially higher (slightly lower) than that for spheres (Koch fractals), for a given snow grain size r_{vp}. Also for the distribution of reflected radiances, spheres differ more from the OHC than Koch fractals do.

The main limitation of the current work is that the SSP parameterization is based on a rather limited observational dataset. The OHC was selected ~~based on~~ using scattering measurements at a single wavelength $\lambda = 0.80\,\mu m$, ~~and~~ for only two cases with blowing snow. This raises several potential issues:

- The choice of the OHC based on scattering measurements only implies that most probably, it does not represent properly the actual distribution of snow grain shapes in blowing snow (or snow on ground). It also neglects the potential dependence of snow grain shapes on their size. Therefore, there is no guarantee that it represents the snow SSPs equally well at other wavelengths, or for all snow grain sizes. ~~Furthermore~~

- Since absorption is very weak at $\lambda = 0.80\,\mu m$, the observations ~~used here~~ do not constrain properly ~~the~~ absorption by snow. Therefore, we cannot expect that our parameterization of β (Eq. 11) predicts precisely the actual values for snow. However, we do expect that it captures reasonably the systematic difference between

non-spherical snow grains and spheres: in general β is larger for non-spherical particles.

- It is also possible that the snow grain shapes, and therefore the SSPs of snow on ground might differ from those of blowing snow, and they might well vary from case to case~~. All this points~~, depending on how much metamorphosis the snow has experienced.

All these issues point to the need for validation of the derived parameterization against actual snow reflectance measurements in future work.

In spite of the concerns mentioned above, it seems reasonable to assume that the OHC selected here provides a substantially better basis for representing the SSPs of snow than spheres do~~, and it may also offer improved accuracy compared to the use of Koch fractals alone~~. Moreover, the ~~parameterizations~~ parameterization equations provided in this paper are analytic and simple to use~~, which should make them an attractive option for use in radiative transfer applications involving snow. A~~. A Fortran implementation of the snow SSP parameterizations is available at https://github.com/praisanen/snow_ssp.

To conclude, this paper describes a first-of-its-kind parameterization for representing the SSPs of snow in the solar spectral region. The parameterization is provided in hope that it will be useful, especially to those researchers that still use spherical particles for computing the radiative effects of snow. Nevertheless, it should definitely not be viewed as the "final solution" to the treatment of SSPs of snow. We hope that the present work will inspire the future development of snow SSP parameterizations based on more comprehensive datasets. Furthermore, at least in principle, it would be desirable to replace the current approach (where the shape distribution of snow grains is selected based on scattering measurements only) with an approach that more directly links the snow grain shapes to those actually observed. This would require, first, the parameterization of the size-shape distribution of snow grains based on observations, and second, the computation and

parameterization of their SSPs. The main challenge in such an approach is the treatment of irregular grains, which are very common in snow.

Appendix A: Extrapolation of single-scattering properties

The largest value of volume-to-projected area equivalent radius for which the SSPs are defined for aggregates of 10 plates in the Yang et al. (2013) database is $r_{\mathrm{vp,max}} = 653\,\mu\mathrm{m}$, which falls below the upper limit of 2000 µm considered for the OHC. Thus, to extend the SSPs for the OHC to sizes up to $r_{\mathrm{vp}} = 2000\,\mu\mathrm{m}$, we extrapolated the SSPs for the aggregates of plates based on how the SSPs depend on size for Koch fractals:

$$Q_{\mathrm{ext,aggregate}}(r_{\mathrm{vp}}) = 2 + [Q_{\mathrm{ext,aggregate}}(r_{\mathrm{vp,lim}}) - 2] \cdot \frac{r_{\mathrm{vp,lim}}}{r_{\mathrm{vp}}}, \tag{A1}$$

$$\beta_{\mathrm{aggregate}}(r_{\mathrm{vp}}) = \beta_{\mathrm{aggregate}}(r_{\mathrm{vp,lim}}) \cdot \frac{\beta_{\mathrm{fractal}}(r_{\mathrm{vp}})}{\beta_{\mathrm{fractal}}(r_{\mathrm{vp,lim}})}, \tag{A2}$$

$$g_{\mathrm{aggregate}}(r_{\mathrm{vp}}) = 1 - [1 - g_{\mathrm{aggregate}}(r_{\mathrm{vp,lim}})] \cdot \frac{1 - g_{\mathrm{fractal}}(r_{\mathrm{vp}})}{1 - g_{\mathrm{fractal}}(r_{\mathrm{vp,lim}})}, \tag{A3}$$

$$P_{11,\mathrm{aggregate}}(r_{\mathrm{vp}}, \theta_{\mathrm{s}}) = P_{11,\mathrm{aggregate}}(r_{\mathrm{vp,lim}}, \theta_{\mathrm{s}}) \cdot \frac{P_{11,\mathrm{fractal}}(r_{\mathrm{vp}}, \theta_{\mathrm{s}})}{P_{11,\mathrm{fractal}}(r_{\mathrm{vp,lim}}, \theta_{\mathrm{s}})}. \tag{A4}$$

Here, $r_{\mathrm{vp,lim}} = 650\,\mu\mathrm{m}$. While this is an ad-hoc approach, the resulting uncertainty in the SSPs for the OHC (in which the aggregates of plates have a weight of 26 %) is most likely small. When the extrapolation was based on droxtals instead of Koch fractals, this changed the values of g by at most 0.0025 and β by at most 0.006 (or 1.4 % in relative terms).

Acknowledgements. P. Räisänen was supported by the Nordic Centre of Excellence for Cryosphere-Atmosphere Interactions in a changing Arctic climate (CRAICC) and the Academy of Finland (grants nos. 140915 and 254195) and T. Nousiainen by the Academy of Finland (grant no. 255718) and the Finnish Funding Agency for Technology and Innovation (Tekes; grant no. 3155/31/2009).

A. Kokhanovsky acknowledges the support of University of Bremen and project CLIMSLIP funded by BMBF. The CLIMSLIP field campaign was funded by the French Agence Nationale de la Recherche (ANR) and the Institut Polaire Français Paul Emile Victor (IPEV). We gratefully acknowledge the NILU and the Norsk Polarinstitutt for their technical assistance during the field campaign at Mount Zeppelin Station. Andreas Macke (Leibniz Institute for Tropospheric Research, Germany) is thanked for making available his ray tracing code. Ping Yang and Bingqi Yi (Texas AM University) are thanked for providing the Yang et al. (2013) database. Last but not least, Bastiaan van Diedenhoven and an anonymous referee are thanked for their helpful comments on the original manuscript.

References

Aoki, T., Aoki, T., Fukabori, M., Hachikubo, A., Tachibana, Y., and Nishio, F.: Effects of snow physical parameters on spectral albedo and bidirectional reflectance of snow surface, J. Geophys. Res., 105, 10219–10236, doi:10.1029/1999JD901122, 2000.

Aoki, T., Katsuyuki, K., Niwano, M., Kodama, Y., Hosaka, M., and Tanaka, T.: Physically based snow albedo model for calculating broadband albedos and the solar heating profile in snowpack for general circulation models, J. Geophys. Res., 116, D11114, doi:10.1029/2010JD015507, 2011.

Barkey, B., Bailey, M., Liou, K., and Hallett, J.: Light-scattering properties of plate and column ice crystals generated in a laboratory cold chamber, Appl. Optics, 41, 5792–5796, 2002.

Baum, B. A., Heymsfield, A. J., Yang, P., and Bedka, S.-T., Bulk scattering properties for the remote sensing of ice clouds. Part I: Microphysical data and models, J. Appl. Meteor., 44, 1885–1895, doi:10.1175/JAM2308.1, 2005.

Baum, B. A., Yang, P., Heymsfield, A. J., Schmitt, C. G., Xie, Y., Bansemer, A., Hu, Y.-X., and Zhang, Z.: Improvements in shortwave bulk scattering and absorption models for the remote sensing of ice clouds, J. Appl. Meteorol. Clim., 50, 1037–1056, doi:10.1175/2010JAMC2608.1, 2011.

Bi, L., Yang, P., Kattawar, G. W., and Kahn, R.: Single-scattering properties of triaxial ellipsoidal particles for a size parameter range from the Rayleigh to geometric-optics regimes, Appl. Optics, 48, 114–126, doi:10.1364/AO.48.000114, 2009.

Bohren, C. F. and Nevitt, T. J.: Absorption by a sphere: a simple approximation, Appl. Optics, 22, 774–775, 1983.

Crépel, O., Gayet, J.-F., Fournol, J.-F., and Oshchepkov, S.: A new airborne Polar Nephelometer for the measurement of optical and microphysical cloud properties. Part II: Preliminary tests, Ann. Geophys., 15, 460–470, doi:10.1007/s00585-997-0460-0, 1997.

de Rooij, W. A. and van der Stap, C. C. A. H.: Expansion of Mie scattering matrices in generalized spherical functions, Astron. Astrophys., 131, 237–248, 1984.

Dubovik, O., Sinuyk, A., Lapyonok, T., Holben, B. N., Mishchenko, M., Yang, P., Eck, T. F., Volten, H., Muñoz, O., Veihelmann, B., van der Zande, W. J., Leon, J.-F., Sorokin, M., and Slutsker, I.: Application of spheroid models to account for aerosol particle nonsphericity in remote sensing of desert dust, J. Geophys. Res., 111, D11208, doi:10.1029/2005JD006619, 2006.

Dubovik, O., Herman, M., Holdak, A., Lapyonok, T., Tanré, D., Deuzé, J. L., Ducos, F., Sinyuk, A., and Lopatin, A.: Statistically optimized inversion algorithm for enhanced retrieval of aerosol properties from spectral multi-angle polarimetric satellite observations, Atmos. Meas. Tech., 4, 975–1018, doi:10.5194/amt-4-975-2011, 2011.

Durand, G., Gayet, J. F., Kaës, L., and Matharan, P.: Airborne infrared and microphysical measurements on cirrus clouds, in: Satellite Remote Sensing of Clouds and the Atmosphere III, P. Soc. Photo-Opt. Ins., 3495, 72–81, 1998.

Flanner, M. G. and Zender, C. S.: Snowpack radiative heating: influence on Tibetan Plateau climate, Geophys. Res. Lett., 32, L06501, doi:10.1029/2004GL022076, 2005.

Francis, P. N., Foot, J. S., and Baran, A. J.: Aircraft measurements of the solar and infrared radiative properties of cirrus and their dependence on ice crystal shape, J. Geophys. Res., 104, 31685–31695, 1999.

Gardner, A. S. and Sharp, M. J.: A review of snow and ice albedo and the development of a new physically based broadband albedo parameterization, J. Geophys. Res., 115, F01009, doi:10.1029/2009JF001444, 2010.

Gayet, J. F., Crépel, O., Fournol, J. F., and Oshchepkov, S.: A new airborne polar Nephelometer for the measurements of optical and microphysical cloud properties. Part I: Theoretical design, Ann. Geophys., 15, 451–459, doi:10.1007/s00585-997-0451-1, 1997.

Gayet, J.-F., Asano, S., Yamazaki, A., Uchiyama, A., Sinyuk, A., Jourdan, O., and Auriol, F.: Two case studies of winter continental-type water and mixed-phase stratocumuli over the sea, 1. Microphysical and optical properties, J. Geophys. Res., 107, 4569, doi:10.1029/2001JD001106 , 2002.

Grenfell, T. C., Warren, S. G., and Mullen, P. C.: Reflection of solar radiation by the Antarctic snow surface at ultraviolet, visible, and near-infrared wavelengths, J. Geophys. Res., 99, 18669–18684, doi:10.1029/94JD01484, 1994.

~~Guyot,~~

Guyot, G., ~~Shcherbakov,V., Jourdan,O~~ O., Olofson, F., Schwarzenboeck, A., ~~Tunved,P., Oloffson,F~~Gourbeyre, C., Febvre, G., Dupuy, R., ~~Febvre,~~Bernard, C., Tunved, P., Ancellet, G., ~~and Gourbeyre,C~~Law, K., Wobrock, W., and Shcherbakov, V.: Ground based in situ measurements of arctic cloud microphysical and optical properties at Mount Zeppelin (Ny-Alesund~~Svalbard): preliminary results~~, Svalbard), in: Proceedings of the ~~Davos Atmosphere and Cryosphere Assembly DACA-13, Davos, Switzerland, 8-12 July 2013, MO-37SUBSCRIPTNBC2.3, 2013.~~ EGU conference, Vienna, Austria, 13–17 April 2015, EGU2015-14794, http://meetingorganizer.copernicus.org/EGU2015/EGU2015-14794.pdf (last access: 1 June 2015), 2015.

Henyey, L. G. and Greenstein, J. L.: Diffuse radiation in the galaxy, Astrophys. J., 93, 70–83, 1941.

Hong, G., Yang P., Baum, B. A., Heymsfield, A. J., and Xu, K.-M.: Parameterization of shortwave and longwave radiative properties of ice clouds for use in climate models, J. Climate, 22, 6287–6312, doi:10.1175/2009JCLI2844.1, 2009.

Jin, Z., Charlock, T. P., Yang, P., Xie, Y., and Miller, W.: Snow optical properties for different particle shapes with application to snow grain size retrieval and MODIS/CERES radiance comparison over Antarctica, Remote Sens. Environ., 112, 3563–3581, 2008.

Jourdan, O., Oshchepkov, S., Shcherbakov, V., Gayet, J.-F., and Isaka, H.: Assessment of cloud optical parameters in the solar region: retrievals from airborne measurements of scattering phase functions, J. Geophys. Res., 108, 4572, doi:10.1029/2003JD003493, 2003.

Jourdan, O., Mioche, G., Garrett, T. J., Schwarzenböck, A., Vidot, J., Xie, Y., Shcherbakov, V., Yang, P., and Gayet, J.-F.: Coupling of the microphysical and optical properties of an Arctic nimbostratus cloud during the ASTAR 2004 experiment: implications for light-scattering modeling, J. Geophys. Res., 115, D23206, doi:10.1029/2010JD014016, 2010.

Kokhanovsky, A. A.: On light scattering in random media with large densely packed particles, J. Geophys. Res., 103, 6089–6096, 1998.

Kokhanovsky, A.: Spectral reflectance of solar light from dirty snow: a simple theoretical model and its validation, The Cryosphere, 7, 1325–1331, doi:10.5194/tc-7-1325-2013, 2013.

Kokhanovsky, A. A. and Nauss, T.: Satellite-based retrieval of ice cloud properties using a semianalytical algorithm, J. Geophys. Res., 110, D19206, doi:10.1029/2004JD005744, 2005.

Kokhanovsky, A. A. and Zege, E. P.: Scattering optics of snow, Appl. Optics, 43, 1589–1602, 2004.
Kokhanovsky, A. A., Aoki, T., Hachikubo, A., Hori, M., and Zege, E. P.: Reflective properties of natural snow: approximate asymptotic theory versus in situ measurements, IEEE Geosci. Remote S., 43, 7, 1529–1535, 2005.
Kokhanovsky, A. A, Rozanov, V. V., Aoki, T., Odermatt, T., Brockmann, C., Krüger, O., Bouvet, M., Drusch, M., and Hori, M.: Sizing snow grains using backscattered solar light, Int. J. Remote Sens., 32, 6975–7008, 2011.
Lawson, R. P., Baker, B. A, Schmitt, C. G., and Jensen, T. L.: An overview of microphysical properties of Arctic clouds observed in May and July 1998 during FIRE ACE, J. Geophys. Res., 106, 14989–15014, doi:10.1029/2000JD900789, 2001.
Levy, R. C., Remer, L. A., and Dubovik, O.: Global aerosol optical properties and application to Moderate Resolution Imaging Spectroradiometer aerosol retrieval over land, J. Geophys. Res., 112, D13210, doi:10.1029/2006JD007815, 2007.
Lyapustin, A., Tedesco, M., Wang, Y., Aoki, T., Hori, M., and Kokhanovsky, A.: Retrieval of snow grain size over Greenland from MODIS, Remote Sens. Environ., 113, 1976–1987, 2009.
Macke, A.: Scattering of light by polyhedral ice crystals, Appl. Optics, 32, 2780–2788, 1993.
Macke, A., Müller, J., and Raschke, E.: Single scattering properties of atmospheric ice crystals, J. Atmos. Sci., 53, 2813–2825, 1996.
Mishchenko, M. I., Dlugach, J. M., Yanovitskij, E. G., and Zakharova, N. T.: Bidirectional reflectance of flat, optically thick particulate layers: an efficient radiative transfer solution and applications to snow and soil surfaces, J. Quant. Spectrosc. Ra., 63, 409–432, 1999.
Muinonen, K., Nousiainen, T., Fast, P., Lumme, K., and Peltoniemi, J. I.: Light scattering by Gaussian random particles: ray optics approximation, J. Quant. Spectrosc. Ra., 55, 577–601, 1996.
Negi, H. S. and Kokhanovsky, A.: Retrieval of snow albedo and grain size using reflectance measurements in Himalayan basin, The Cryosphere, 5, 203–217, doi:10.5194/tc-5-203-2011, 2011.
Nousiainen, T. and McFarquhar, G. M.: Light scattering by quasi-spherical ice crystals, J. Atmos. Sci., 61, 2229–2248, 2004.
Nousiainen, T. and Muinonen, K.: Light scattering by Gaussian, randomly oscillating raindrops, J. Quant. Spectrosc. Ra., 63, 643–666, 1999.
Nousiainen, T., Lindqvist, H., McFarquhar, G. M., and Um, J.: Small irregular ice crystals in tropical cirrus, J. Atmos. Sci., 68, 2614–2627, 2011.
Shcherbakov, V., Gayet, J.-F., Baker, B., and Lawson, P.: Light scattering by single natural ice crystals, J. Atmos. Sci., 63, 1513–1525, doi:10.1175/JAS3690.1, 2006.

Smith, H. R., Connolly, P. J., Baran, A. J., Hesse, E., Smedley, A. R. D., and Webb, A. R.: Cloud chamber laboratory investigations into scattering properties of hollow ice particles, J. Quant. Spectrosc. Ra., 157, 106–118, doi:10.1016/j.jqsrt.2015.02.015, 2015.

Stamnes, K., Tsay, S. C., Wiscombe, W., and Jayaweera, K.: Numerically stable algorithm for discrete-ordinate-method radiative transfer in multiple scattering and emitting layered media, Appl. Optics, 27, 2502–2509, 1988.

Tanikawa T., Aoki, T., Hori, M., Hachikubo, A., and Aniya, M.: Snow bidirectional reflectance model using non-spherical snow particles and its validation with field measurements, EARSeLeProceedings, 5, 137–145, http://www.eproceedings.org/static/vol05_2/05_2_tanikawa1.html (last access: 1 June 2015), 2006.

van Diedenhoven, B., Ackerman, A. S., Cairns, B., and Fridlind, A. M.: A flexible parameterization for shortwave optical properties of ice crystals, J. Atmos. Sci., 71, 1763–1782, doi:10.1175/JAS-D-13-0205.1, 2014.

Wang, Z. and Zeng, X.: Evaluation of snow albedo in land models for weather and climate studies, J. Appl. Meteorol. Clim., 49, 363–380, 2010.

Warren, S. G. and Brandt, R. E.: Optical constants of ice from the ultraviolet to the microwave: a revised compilation, J. Geophys. Res., 113, D14220, doi:10.1029/2007JD009744, 2008.

Wiscombe, W. J.: The delta-M method: rapid yet accurate radiative flux calculations for strongly asymmetric phase functions, J. Atmos. Sci., 34, 1408–1422, 1977.

Wiscombe, W. J. and Warren, S. G.: A model for the spectral albedo of snow. I: Pure snow, J. Atmos. Sci., 37, 2712–2733, 1981.

Xie, Y., Yang, P., Gao, B.-C., Kattawar, G. W., and Mishchenko, M. I.: Effect of ice crystal shape and effective size on snow bidirectional reflectance, J. Quant. Spectrosc. Ra., 100, 457–469, doi:10.1016/j.jqsrt.2005.11.056, 2006.

Yang, P. and Liou, K.-N.: Single-scattering properties of complex ice crystals in terrestrial atmospheres, Contributions to Atmospheric Physics, 71, 223–248, 1998.

Yang, P., Bi, L., Baum, B. A., Liou, K.-N., Kattawar, G. W., Mishchenko, M. I., and Cole, B.: Spectrally consistent scattering, absorption and polarization of atmospheric ice crystals at wavelengths from 0.2 to 100 µm, J. Atmos. Sci., 70, 330–347, 2013.

Yurkin, M. A., Maltsev, V. P., and Hoekstra, A. G.: The discrete dipole approximation for simulation of light scattering by particles much larger than the wavelength, J. Quant. Spectrosc. Ra., 106, 546–557, 2007.

Zege, E. P., Katsev, I. L., Malinka, A. V., Prikhach, A. S., Heygster, G., and Wiebe, H.: Algorithm for retrieval of the effective snow grain size and pollution amount from satellite measurements, Remote Sens. Environ., 115, 2674–2685, 2011.

Table 1. List of best three-habit combinations. w_1, w_2 and w_3 are the weights (i.e., fractional contributions to projected area) of each habit, "cost" is the cost function, g the asymmetry parameter, and ξ a non-dimensional absorption parameter defined by Eq. (8). SR refers to severely rough particles, and t is the distortion parameter for 2nd generation Koch fractals. The "optimed habit combination" (OHC) is highlighted with *italic font*.

w_1	habit$_1$	w_2	habit$_2$	w_3	habit$_3$	cost	g	ξ
0.38	fractal ($t = 0.50$)	0.32	SR droxtal	0.30	SR hollow column	0.084	0.777	1.64
0.38	fractal ($t = 0.50$)	0.26	SR droxtal	0.36	SR hollow bullet rosette	0.085	0.777	1.65
0.38	*fractal ($t = 0.50$)*	*0.36*	*SR droxtal*	*0.26*	*aggregate (10 SR plates)*	*0.086*	*0.778*	*1.62*
0.30	fractal ($t = 0.50$)	0.34	SR droxtal	0.36	aggregate (5 SR plates)	0.086	0.778	1.60
0.46	fractal ($t = 0.50$)	0.36	SR droxtal	0.18	SR plate	0.087	0.778	1.66
0.38	fractal ($t = 0.50$)	0.28	SR droxtal	0.34	SR solid column	0.090	0.776	1.63
0.42	fractal ($t = 0.18$)	0.26	SR droxtal	0.32	SR hollow bullet rosette	0.095	0.779	1.66
0.42	fractal ($t = 0.18$)	0.32	SR droxtal	0.26	SR hollow column	0.095	0.778	1.65
0.34	fractal ($t = 0.18$)	0.32	SR droxtal	0.34	aggregate (5 SR plates)	0.096	0.779	1.61
0.42	fractal ($t = 0.18$)	0.34	SR droxtal	0.24	aggregate (10 SR plates)	0.098	0.780	1.63

Table 2. Parameterization coefficients appearing in Eq. (27).

	c_{1n}	c_{2n}	c_{3n}	c_{4n}
$n=0$	0.00000	0.00000	0.00000	0.00000
$n=1$	0.00000	0.00000	0.00000	0.00000
$n=2$	−0.01400	−0.10367	0.02144	0.08903
$n=3$	−0.13184	−0.01741	0.16890	−0.06365
$n=4$	−0.20878	−0.03438	0.27353	−0.10418
$n=5$	−0.29763	−0.06931	0.38501	−0.11329
$n=6$	−0.32153	−0.10691	0.41282	−0.07934

Table 3. Parameterization coefficients appearing in Eq. (29).

	d_{1n}	d_{2n}	d_{3n}	d_{4n}
$n=0$	−0.06679	0.34357	0.09553	−0.42542
$n=1$	−0.53413	0.15642	0.74905	−0.62700
$n=2$	−1.49866	−2.42334	1.76580	2.10118
$n=3$	1.01884	−2.05239	−1.59160	3.54237
$n=4$	4.43936	2.85558	−5.48475	−0.97817
$n=5$	2.07065	3.25673	−2.40933	−2.94094

Table A1. List of abbreviations and symbols.

CLIMSLIP	CLimate IMpacts of Short-Lived pollutants In the Polar region
CPI	cloud particle imager
CS	completely smooth particles (Yang et al., 2013)
DISORT	Discrete Ordinates Radiative Transfer Program for a Multi-Layered Plane-Parallel Medium (Stamnes et al., 1988)
HG	Henyey–Greenstein (Henyey and Greenstein, 1941)
LAPACK	Linear Algebra Package
LOGRMSE	root-mean-square error in the logarithm of reflected radiances
MR	moderately rough particles (Yang et al., 2013)
OHC	optimized habit combination
PN	polar nephelometer
SSP	single-scattering properties
SR	severely rough particles (Yang et al., 2013)
β	single-scattering co-albedo = 1 $-$ single-scattering albedo
δ	Dirac's delta function
θ	zenith angle
θ_0	zenith angle for incident radiation
θ_s	scattering angle
λ	wavelength
μ_0	cosine of zenith angle for incident radiation
ν	power-law index in the Legendre polynomial expansion of the correlation function of radius for Gaussian random spheres
ξ	non-dimensional absorption parameter (Eq. 8)
σ	relative SD of radius for Gaussian random spheres
ϕ	azimuth angle
ω	single-scattering albedo
f	truncated fraction of phase function in δ-M-scaling (Wiscombe, 1977)
g	asymmetry parameter
g_1	asymmetry parameter for the Henyey–Greenstein part in Eq. (21), defined by Eq. (24)
g_{diff}	asymmetry parameter for diffraction (Eq. 19)
g_{ray}	asymmetry parameter for the ray-tracing part (Eq. 23)
l_{max}	degree of truncation of the Legendre polynomial expansion of the correlation function of radius for Gaussian random spheres
m_{i}	imaginary part of refractive index
m_{r}	real part of refractive index
P	projected area
P_{11}	phase function
P_{11}^{ref}	reference phase function constructed from CLIMSLIP data (Eq. 2)
P_{11}^{OHC}	phase function for the optimized habit combination
P_{HG}	Henyey–Greenstein phase function (Eqs. 18, 20)
P_{diff}	parameterized phase function for diffraction (Eq. 17)
P_{ray}	parameterized phase function for the ray tracing part (Eq. 21)
P_{resid}	residual in the phase function parameterization (Eq. 25)
P_{resid}^{*}	residual in the phase function parameterization, truncated for δ-M-scaling (Eqs. 26, 28)
P_n	nth order Legendre polynomial
Q_{ext}	extinction efficiency
r_{vp}	volume-to-projected area equivalent radius
t	degree of distortion for Koch fractals
V	volume
w_1	weight factor for the Henyey–Greenstein part in Eq. (21), defined by Eq. (22)
w_{diff}	weight factor for the diffraction part in the parameterized phase function (Eqs. 14, 30), defined by Eq. (15)
w_{ray}	weight factor for the ray tracing part in the parameterized phase function (Eqs. 14, 30), defined by Eq. (16)
x	size parameter
x_{abs}	size parameter for absorption (Eq. 12)
x_{p}	size parameter defined with respect to the projected area equivalent radius
x_{vp}	size parameter defined with respect to the volume-to-projected area equivalent radius (Eq. 10)

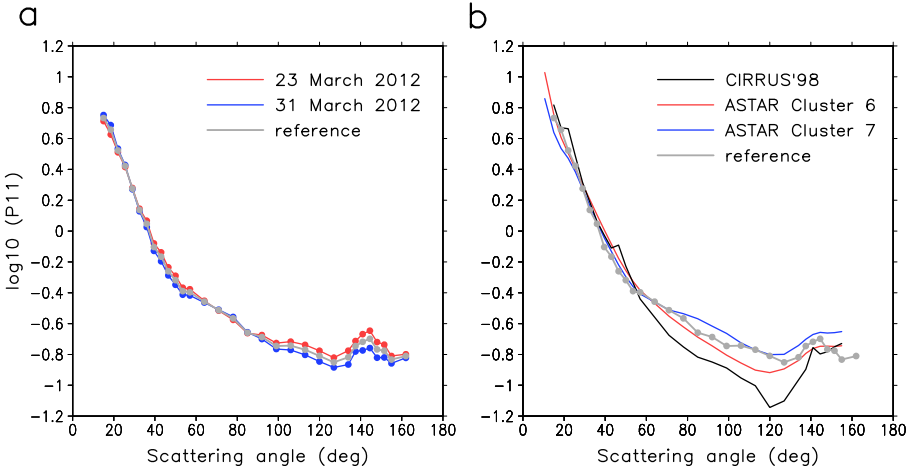

Figure 1. (a) Phase function of blowing snow as derived from the CLIMSLIP data on 23 March 2012 (red) and on 31 March 2012 (blue). The reference phase function P_{11}^{ref} (grey) was defined as the average of the 23 and 31 March cases. **(b)** Comparison of P_{11}^{ref} with phase functions for non-precipitating cirrus (CIRRUS'98, black line) and glaciated Arctic nimbostratus (ASTAR Clusters 6 and 7, red and blue lines).

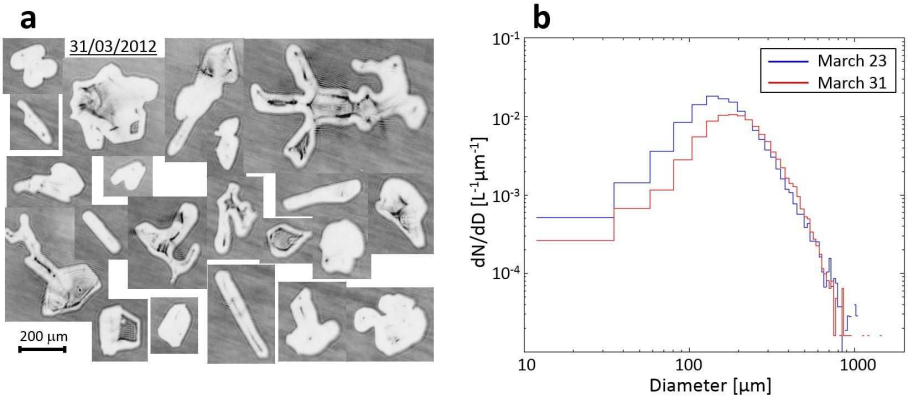

Figure 2. (a) Examples of snow ~~crystals~~ grains imaged by the CPI instrument on 31 March 2012 and **(b)** size distributions for both the 23 and 31 March cases.

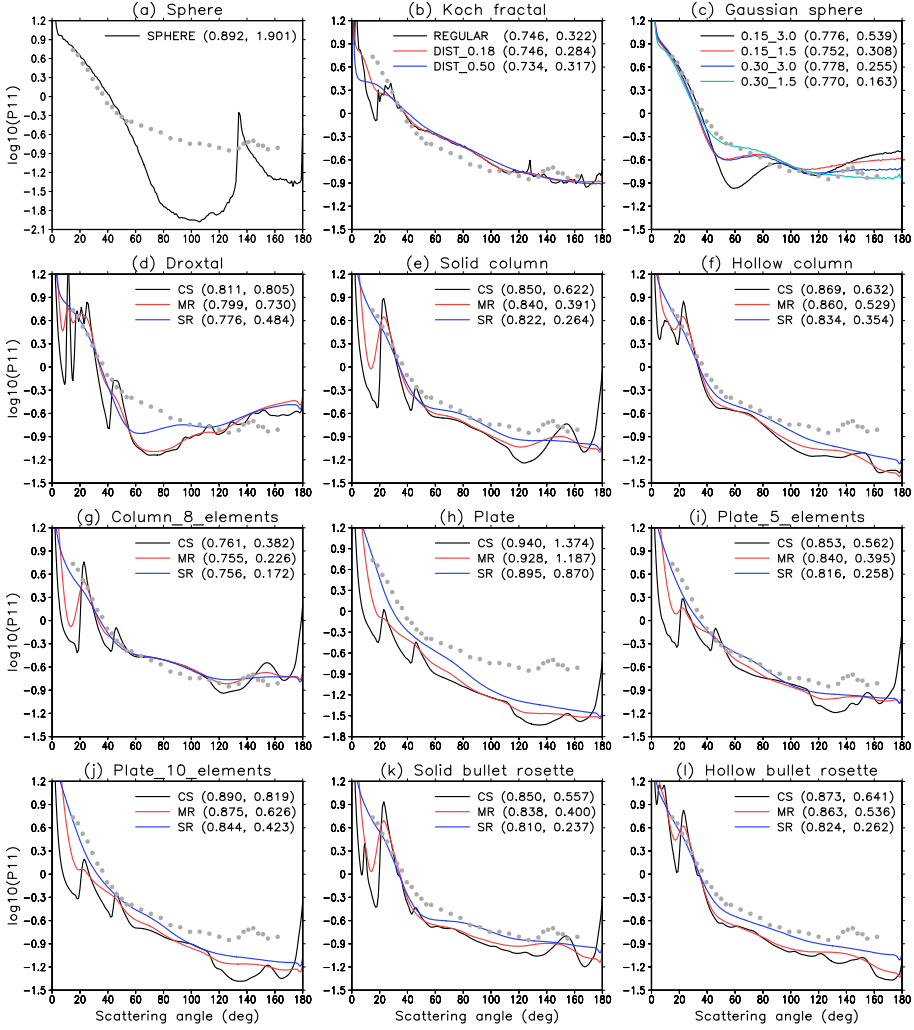
(a) Sphere
SPHERE (0.892, 1.901)
(b) Koch fractal
REGULAR (0.746, 0.322)
DIST_0.18 (0.746, 0.284)
DIST_0.50 (0.734, 0.317)
(c) Gaussian sphere
0.15_3.0 (0.776, 0.539)
0.15_1.5 (0.752, 0.308)
0.30_3.0 (0.778, 0.255)
0.30_1.5 (0.770, 0.163)
(d) Droxtal
CS (0.811, 0.805)
MR (0.799, 0.730)
SR (0.776, 0.484)
(e) Solid column
CS (0.850, 0.622)
MR (0.840, 0.391)
SR (0.822, 0.264)
(f) Hollow column
CS (0.869, 0.632)
MR (0.860, 0.529)
SR (0.834, 0.354)
(g) Column_8_elements
CS (0.761, 0.382)
MR (0.755, 0.226)
SR (0.756, 0.172)
(h) Plate
CS (0.940, 1.374)
MR (0.928, 1.187)
SR (0.895, 0.870)
(i) Plate_5_elements
CS (0.853, 0.562)
MR (0.840, 0.395)
SR (0.816, 0.258)
(j) Plate_10_elements
CS (0.890, 0.819)
MR (0.875, 0.626)
SR (0.844, 0.423)
(k) Solid bullet rosette
CS (0.850, 0.557)
MR (0.838, 0.400)
SR (0.810, 0.237)
(l) Hollow bullet rosette
CS (0.873, 0.641)
MR (0.863, 0.536)
SR (0.824, 0.262)
log10(P11)
Scattering angle (deg)

Figure 3. Comparison of phase function for various shape models with the reference phase function derived from CLIMSLIP data (P_{11}^{ref} shown with gray dots in each panel). **(a)** Spheres, **(b)** regular and distorted 2nd generation Koch fractals (with distortion parameters $t = 0.18$ and $t = 0.50$), **(c)** four realizations of Gaussian spheres, and **(d–l)** nine habits in the Yang et al. (2013) database. For each habit, the phase function was averaged over the size distribution defined by Eq. (3). In the figure legends, the two numbers in parentheses give the asymmetry parameter and the cost function defined by Eq. (4), respectively. For the Gaussian spheres in **(c)**, the notation indicates the shape parameters (e.g., for 0.15_3.0, $\sigma = 0.15$ and $\nu = 3.0$); l_{max} was fixed at 15. For the Yang et al. (2013) habits in **(d–l)**, CS, MR and SR refer to particles with completely smooth surface, moderate surface roughness, and severe surface roughness, respectively.

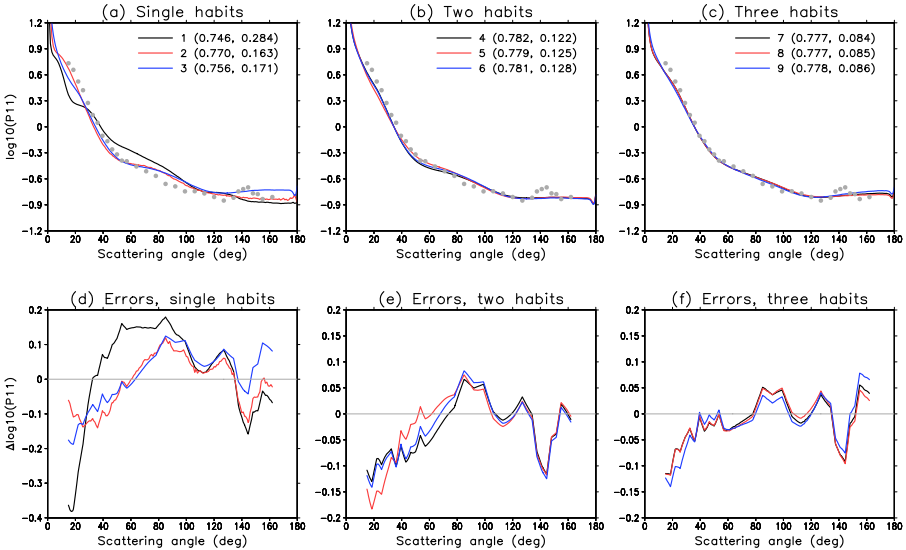

Figure 4. Comparison of modeled phase functions with the reference phase function (P_{11}^{ref} shown with gray dots in **a–c**). **(a)** Selected single-habit cases: 1 = distorted Koch fractals with $t = 0.18$; 2 = Gaussian spheres with $\sigma = 0.30$, $\nu = 1.5$ and $l_{\mathrm{max}} = 15$; and 3 = aggregates of 8 severely rough (SR) ~~aggregates of 8~~ columns. **(b)** Best combinations of two habits: 4 = aggregates of 8 SR columns and SR hollow bullet rosettes (weights 0.61 and 0.39); 5 = aggregates of 8 SR columns and aggregates of 5 SR plates (weights 0.61 and 0.39); and 6 = aggregates of 8 SR columns and SR hollow columns (weights 0.68 and 0.32). **(c)** Best combinations of three habits: 7 = SR droxtals, SR hollow columns and distorted Koch fractals ($t = 0.50$) (weights 0.32, 0.30 and 0.38); 8 = SR droxtals, SR hollow bullet rosettes and distorted Koch fractals ($t = 0.50$) (weights 0.26, 0.36 and 0.38); and 9 = SR droxtals, aggregates of 10 SR plates and distorted Koch fractals ($t = 0.50$) (weights 0.36, 0.26 and 0.38). In the legends in **(a–c)**, the two numbers in parentheses give the asymmetry parameter and the cost function defined by Eq. (4), respectively. **(d–f)** show the corresponding differences from P_{11}^{ref}.

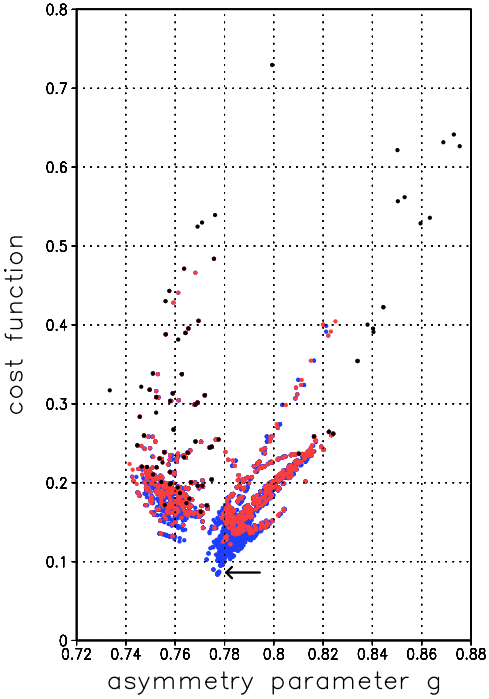

Figure 5. ~~**(a)**~~ A scatter plot of asymmetry parameter vs. cost function (Eq. 4) for single habits (black dots), for combinations of two habits (red dots), and for combinations of three habits (blue dots). The "optimized habit combination" selected for parameterization of snow single-scattering properties is marked with an arrow. ~~**(b)** Same as **(a)**, but for the non-dimensional absorption parameter ζ vs. cost function (see Eq. 8).~~ Note that some single-habit cases fall outside the range plotted here. These include spheres, for which cost $= 1.90$ ~~,~~ and $g = 0.892$~~, and $\zeta = 1.29$~~.

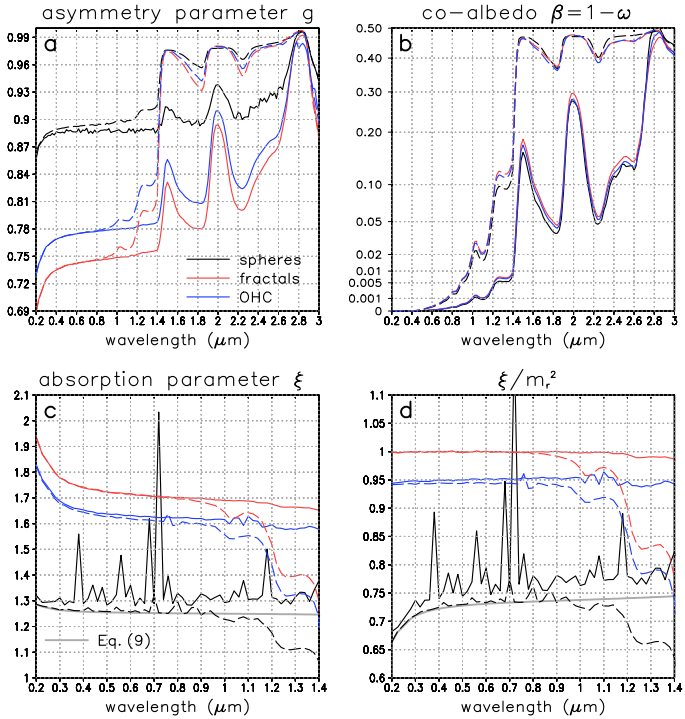

Figure 6. Comparison of single-scattering properties for spheres (black lines), distorted Koch fractals with $t = 0.18$ (red), and the optimized habit combination (blue), for $r_{vp} = 50\,\mu m$ (solid lines) and $r_{vp} = 1000\,\mu m$ (dashed lines), for a monodisperse size distribution. **(a)** Asymmetry parameter g; **(b)** single-scattering co-albedo $\beta = 1 - \omega$; **(c)** non-dimensional absorption parameter ξ (Eq. 8); and **(d)** ξ divided by the real part of refractive index squared. In (**c** and **d**), the grey line represents Eq. (9).

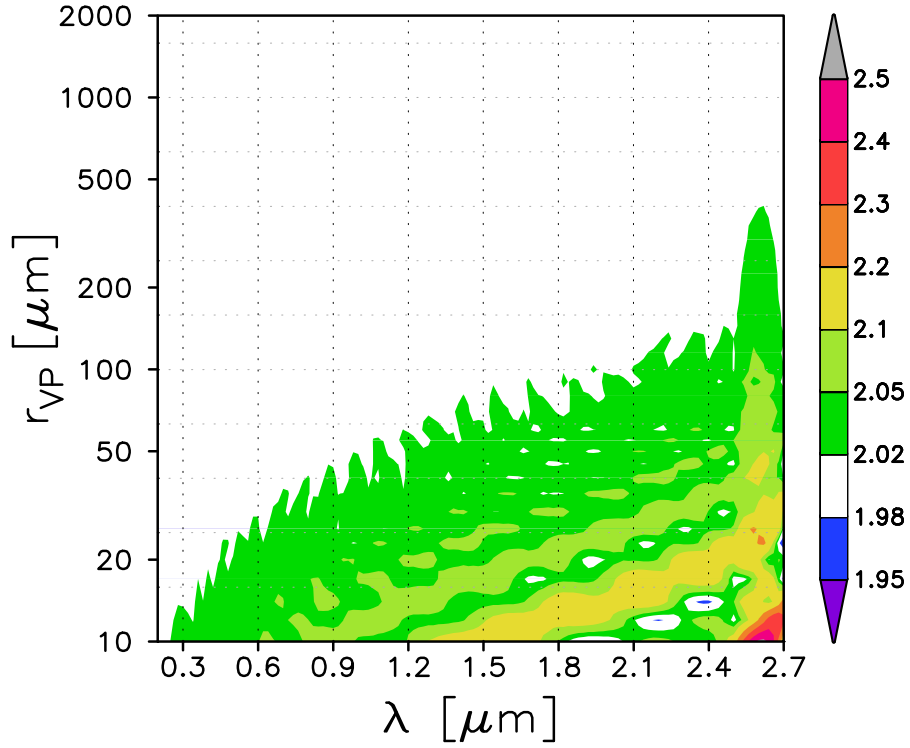

Figure 7. Extinction efficiency Q_{ext} for the optimized habit combination as a function of wavelength (λ) and volume-to-projected area equivalent radius (r_{vp}).

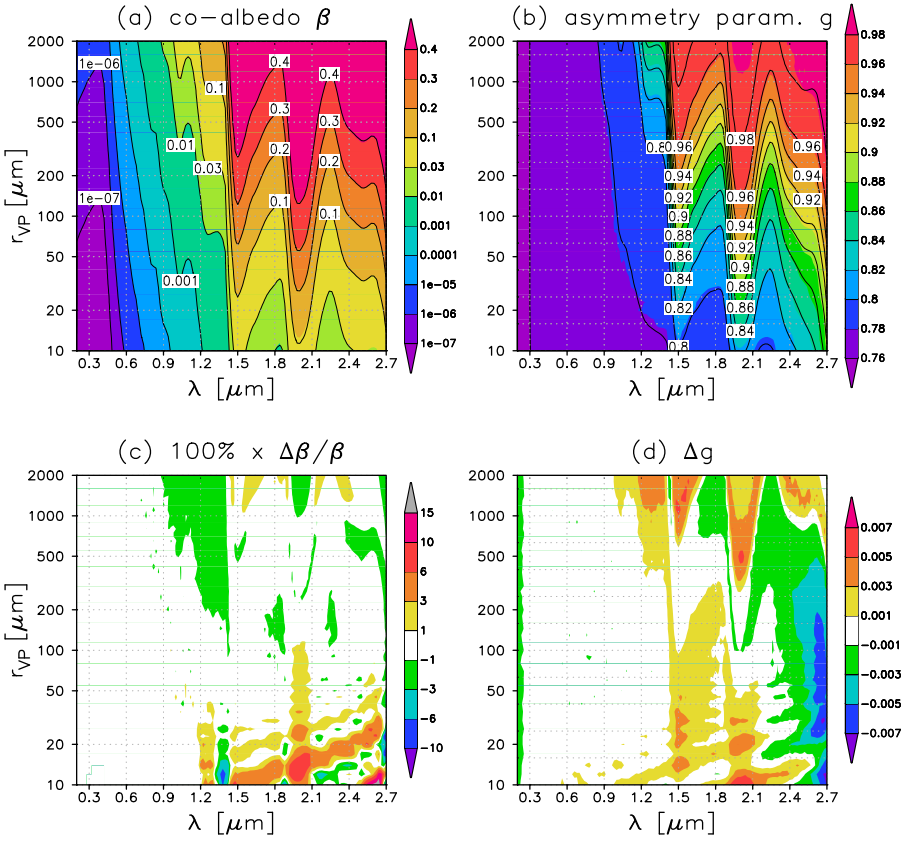

Figure 8. Comparison of **(a)** parameterized single-scattering co-albedo β (contours) with the reference values computed for the OHC (shading), and **(b)** parameterized asymmetry parameter g (contours) with the reference values (shading). **(c)** Relative errors (%) in the parameterized co-albedo. **(d)** Absolute errors in the parameterized asymmetry parameter.

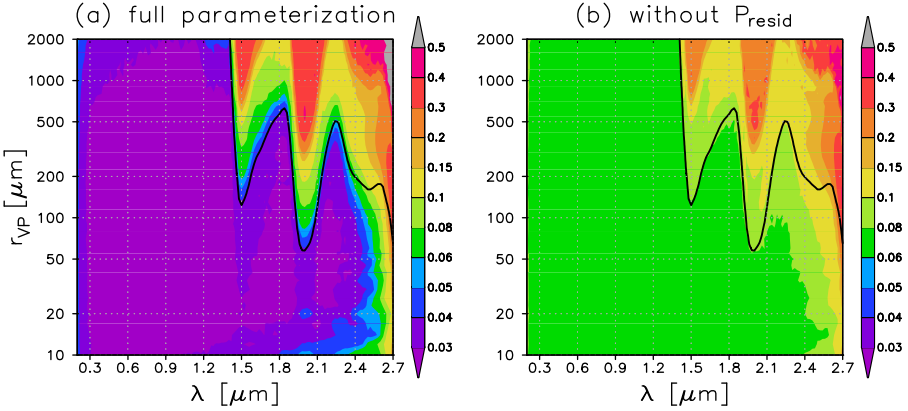

Figure 9. Cost function for the phase function parameterization as defined by Eq. (32) for **(a)** the full parameterization (Eq. 14) and **(b)** without the term P_{resid}. The black solid line indicates, for reference, a co-albedo value of $\beta = 0.3$, which approximately corresponds to a spherical albedo of 0.03 for an optically thick snow layer.

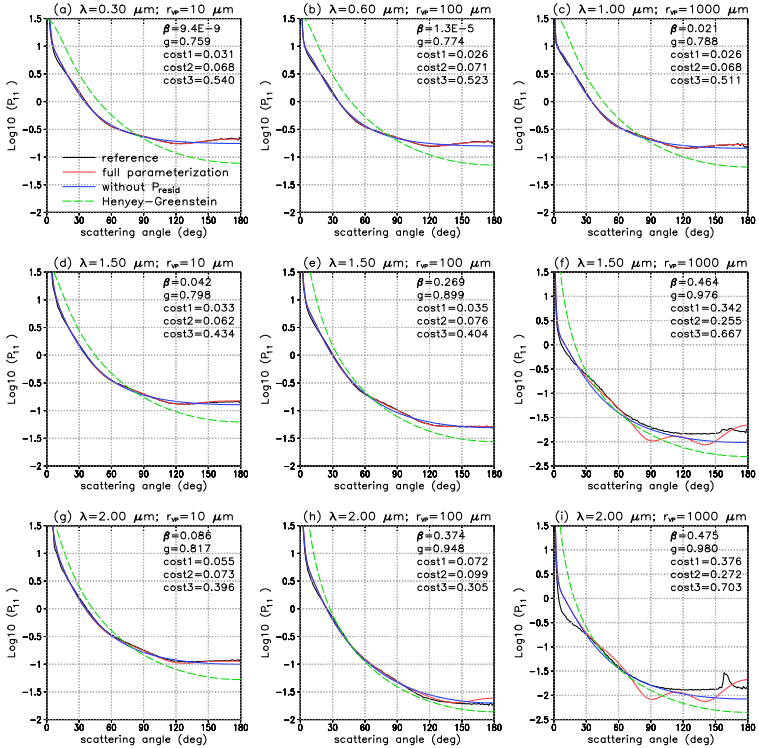

Figure 10. Examples of the reference phase function computed for the OHC (black lines) and of the parameterized phase function for the full parameterization (red lines) ~~and~~, the simplified parameterization without the term P_{resid} in Eq. (14) (blue lines), and the Henyey-Greenstein phase function with asymmetry parameter defined by Eq. (13) (dashed green lines) for nine combinations of wavelength λ and volume-to-projected area equivalent radius r_{vp}. For reference, the values of single-scattering co-albedo β, asymmetry parameter g, and cost functions for the full parameterization (cost1) ~~and~~, for the simplified parameterization (cost2) and for the Henyey-Greenstein phase function (cost3) are listed in each panel.

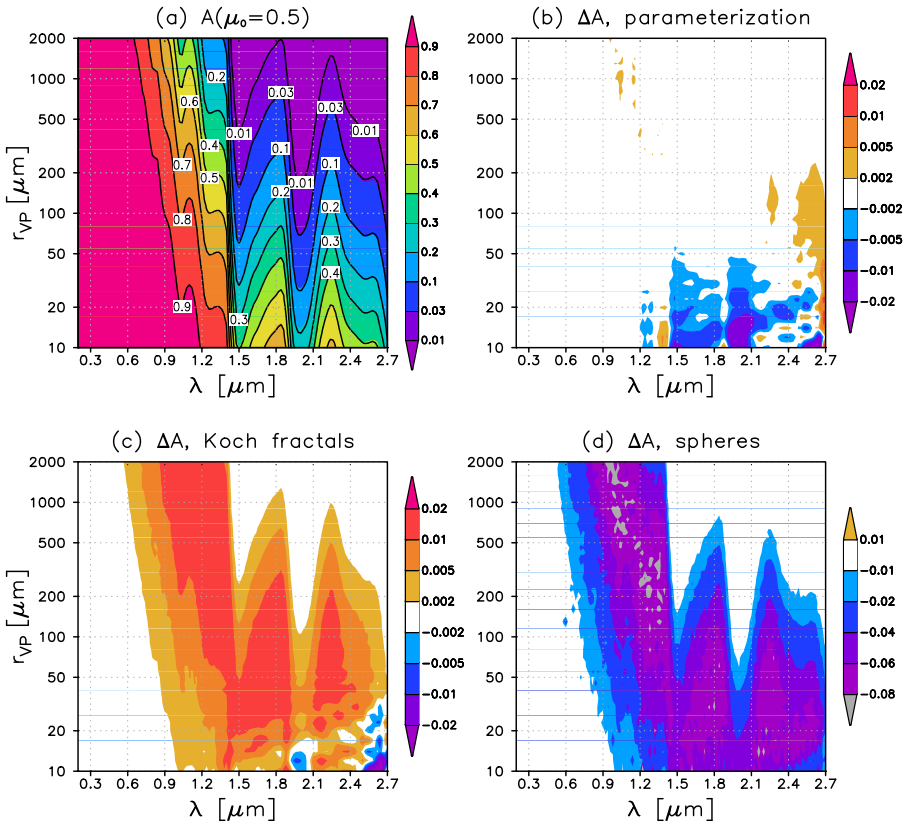

Figure 11. Albedo of a semi-infinite snow layer for direct incident radiation with the cosine of zenith angle $\mu_0 = 0.5$. **(a)** Reference values computed for the OHC (shading) and values for the full snow optics parameterization (contours). **(b)** The difference between the parameterization and the reference, **(c)** between distorted Koch fractals ($t = 0.18$) and the reference, and **(d)** between spheres and the reference. Note that the colour scale differs between the figure panels.

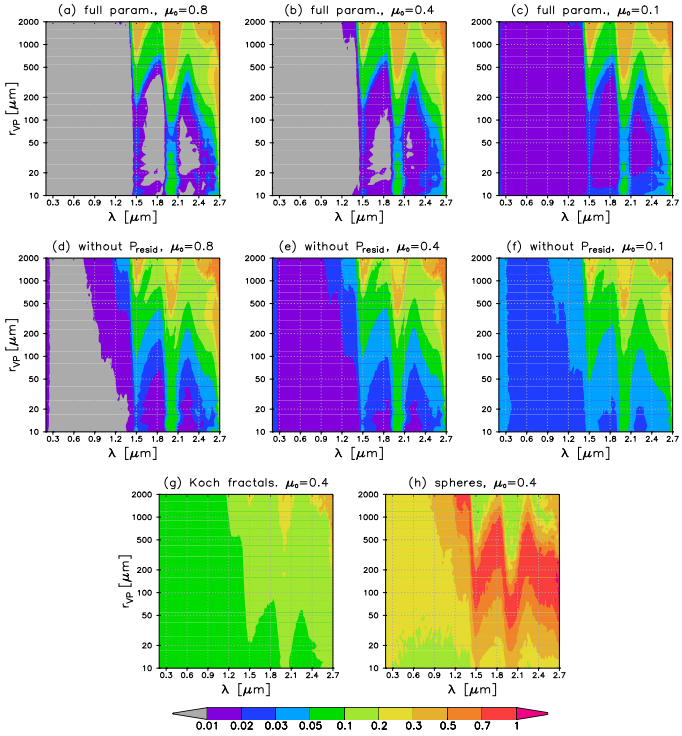

Figure 12. Root-mean square errors in ln(radiance) (Eq. 33) for **(a–c)** the full parameterization and **(d–f)** the simpler parameterization without the term P_{resid} in the phase function, as compared with reference calculations for the OHC, for three directions of incident radiation (cosine of zenith angle $\mu_0 = 0.8$, $\mu_0 = 0.4$, and $\mu_0 = 0.1$, respectively). (**g** and **h**) show the respective differences from the reference calculations for distorted Koch fractals ($t = 0.18$) and spheres (for $\mu_0 = 0.4$ only).

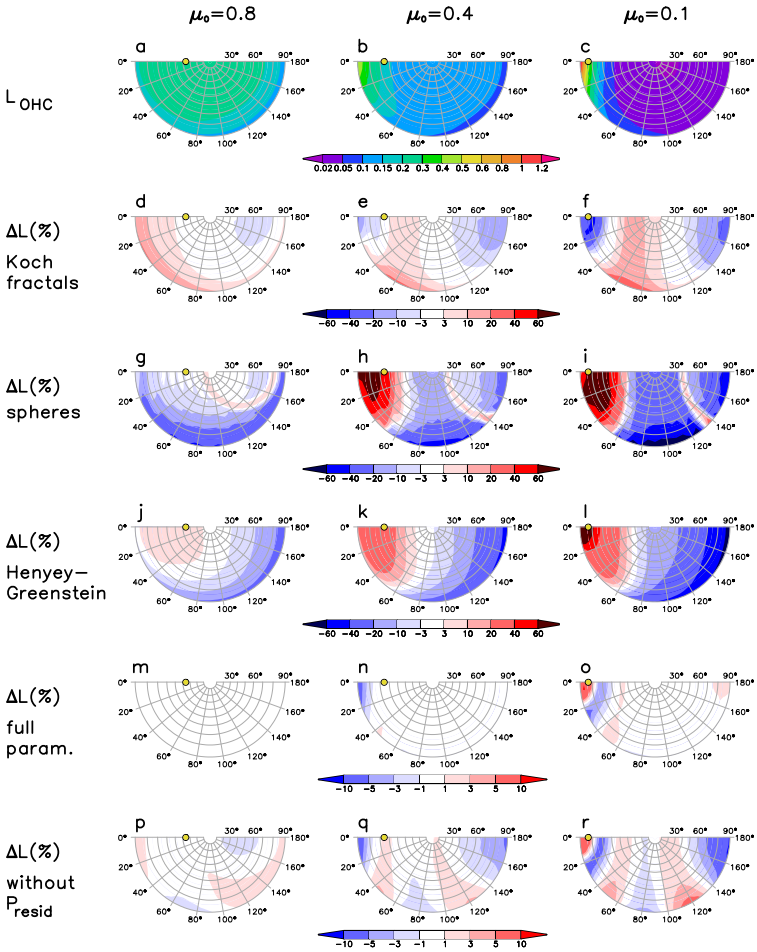
μ_0=0.8
μ_0=0.4
μ_0=0.1
L_{OHC}
ΔL(%) Koch fractals
ΔL(%) spheres
ΔL(%) Henyey–Greenstein
ΔL(%) full param.
ΔL(%) without P_{resid}
0.02 0.05 0.1 0.15 0.2 0.3 0.4 0.5 0.6 0.8 1 1.2
−60 −40 −20 −10 −3 3 10 20 40 60
−10 −5 −3 −1 1 3 5 10

Figure 13. (a–c) Angular distribution of reflected radiances for the OHC for a single wavelength $\lambda = 0.80\,\mu m$ and a single particle size $r_{vp} = 200\,\mu m$. The yellow sphere indicates the cosine of zenith angle for the incident radiation ($\mu_0 = 0.8$, $\mu_0 = 0.4$ and $\mu_0 = 0.1$ for **(a–c)**, respectively). The azimuth angle for the incident radiation is $\phi_0 = 0°$. **(d–f)** and **(g–i)** show the fractional differences in reflected radiances (in %) from the OHC for distorted Koch fractals with $t = 0.18$ and for ice spheres, respectively. **(j–l)** ~~and **(m–o)**~~ show the differences from the OHC for the Henyey-Greenstein phase function (with g computed using Eq. 13 and β using Eq. 11), **(m–o)** for the full snow optics parameterization and **(p–r)** for the simpler parameterization without P_{resid} in Eq. (14). Note that the colour scale in **(m–r)** differs from that in **(d–l)**.

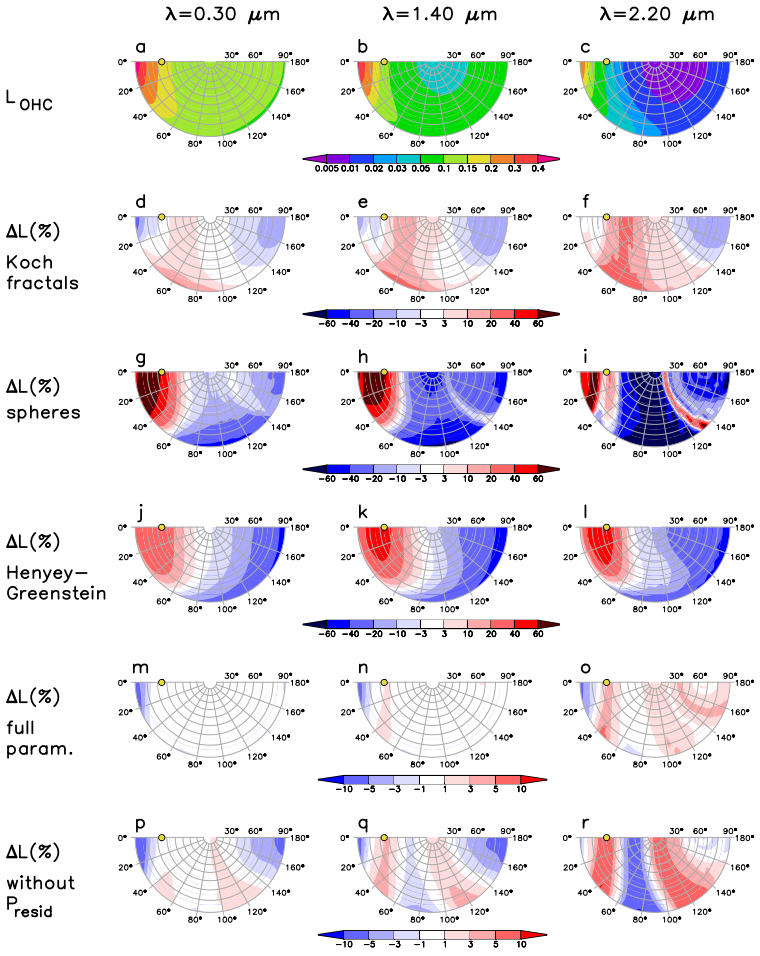

Figure 14. As Fig. 13, but for three wavelengths $\lambda = 0.30$, 1.40 and ~~2.00~~2.20 µm, for a single value of the cosine of zenith angle for incident radiation $\mu_0 = 0.4$ and a single particle size $r_{vp} = 200$ µm.